Pergamon

Int. J. Solids Structures Vol. 32, No. 12, pp. 1675–1710, 1995
Elsevier Science Ltd
Printed in Great Britain

0020–7683(94)00201–0

THERMO-INELASTIC RESPONSE OF FUNCTIONALLY GRADED COMPOSITES

JACOB ABOUDI† and MAREK-JERZY PINDERA
University of Virginia, Charlottesville, Virginia, U.S.A.

and

STEVEN M. ARNOLD
National Aeronautics and Space Administration, Lewis Research Center, Cleveland, Ohio, U.S.A.

(*Received* 1 *April* 1994; *in revised form* 18 *August* 1994)

Abstract—A recently developed micromechanical theory for the thermo-elastic response of functionally graded composites is further extended to include the inelastic and temperature-dependent response of the constituent phases. In contrast to currently employed micromechanical approaches applied to this newly emerging class of materials, which decouple the local and global effects by assuming the existence of a representative volume element at every point within the composite, the new theory explicitly couples the local and global effects. Previous thermo-elastic analysis has demonstrated that such coupling is necessary when: the temperature gradient is large with respect to the dimension of the inclusion phase; the characteristic dimension of the inclusion phase is large relative to the global dimensions of the composite; and the number of inclusions is small. In these circumstances, the concept of the representative volume element is no longer applicable and the standard micromechanical analyses based on this concept produce questionable results. Examples of composite materials that fall into this category include large-diameter fiber composites such as SiC/Ti and B/Al. Herein, we extend this new approach to include the inelastic and temperature-dependent response of the constituent phases in order to be able to realistically model functionally graded metal matrix composites in the presence of large temperature gradients. The inelastic behavior of the matrix phase is modeled using two inelastic models, namely the Bodner–Partom unified viscoplasticity theory and the classical incremental plasticity theory. Results are presented that illustrate the differences between elastic and inelastic analyses, defining under what circumstances the inclusion of inelastic effects is important. Application of the theory to composites with thermal barrier coatings demonstrates the utility of the concept of *internal temperature management* through functional grading of the microstructure using differently-distributed particulate inclusions.

NOMENCLATURE

p, q, r	indices used to identify the cell (p, q, r)
α, β, γ	indices used to identify the subcell $(\alpha\beta\gamma)$
$d_\alpha^{(p)}, h_\beta, l_\gamma$	dimensions of the subcell $(\alpha\beta\gamma)$ in the pth unit cell
$v_{(\alpha\beta\gamma)}^{(p)}$	volume of the subcell $(\alpha\beta\gamma)$
$\bar{x}_1^{(\alpha)}, \bar{x}_2^{(\beta)}, \bar{x}_3^{(\gamma)}$	local subcell coordinates
$k_i^{(\alpha\beta\gamma)}$	coefficients of heat conductivity of the material in the subcell $(\alpha\beta\gamma)$
$T^{(\alpha\beta\gamma)}$	temperature field in the subcell $(\alpha\beta\gamma)$
$T_0^{(\alpha\beta\gamma)}$	temperature at the center of the subcell $(\alpha\beta\gamma)$
$T_i^{(\alpha\beta\gamma)}$	coefficients in the temperature expansion within the subcell $(\alpha\beta\gamma)$
$q_i^{(\alpha\beta\gamma)}$	components of the heat flux vector in the subcell $(\alpha\beta\gamma)$
$u_i^{(\alpha\beta\gamma)}$	displacement components in the subcell $(\alpha\beta\gamma)$
$w_1^{(\alpha\beta\gamma)}$	x_1 displacement component at the center of the subcell $(\alpha\beta\gamma)$
$\phi_1^{(\alpha\beta\gamma)}$	coefficients associated with the linear terms in the second-order expansion of the subcell displacement $u_1^{(\alpha\beta\gamma)}$
$\varkappa_2^{(\alpha\beta\gamma)}$	coefficients associated with the linear terms in the first-order expansion of the subcell displacement $u_2^{(\alpha\beta\gamma)}$
$\Psi_3^{(\alpha\beta\gamma)}$	coefficients associated with the linear terms in the first-order expansion of the subcell displacement $u_3^{(\alpha\beta\gamma)}$
$U_1^{(\alpha\beta\gamma)}$	coefficients associated with the quadratic term $x_1^{(\alpha)2}$ in the second-order expansion of the subcell displacement $u_1^{(\alpha\beta\gamma)}$

† Visiting Professor, Faculty of Engineering, Tel-Aviv University, Ramat-Aviv 69978, Israel

$V_1^{(\alpha\beta\gamma)}$ coefficients associated with the quadratic term $x_2^{(\beta)2}$ in the second-order expansion of the subcell displacement $u_1^{(\alpha\beta\gamma)}$

$W_1^{(\alpha\beta\gamma)}$ coefficients associated with the quadratic term $x_3^{(\gamma)2}$ in the second-order expansion of the subcell displacement $u_1^{(\alpha\beta\gamma)}$

$\varepsilon_{ij}^{(\alpha\beta\gamma)}$ local strain components in the subcell $(\alpha\beta\gamma)$

$\sigma_{ij}^{(\alpha\beta\gamma)}$ local stress components in the subcell $(\alpha\beta\gamma)$

$c_{ijkl}^{(\alpha\beta\gamma)}$ elements of the stiffness tensor of the material in the subcell $(\alpha\beta\gamma)$

$\Gamma_{ij}^{(\alpha\beta\gamma)}$ elements of the thermal tensor of the material in the subcell $(\alpha\beta\gamma)$ (products of the stiffness tensor and the thermal expansion coefficients)

$S_{ij(l,m,n)}^{(\alpha\beta\gamma)}$ average values of the subcell stress components $\sigma_{ij}^{(\alpha\beta\gamma)}$ when $l = m = n = 0$; higher-order stress components for other values of l, m, n

$\mu_{(\alpha\beta\gamma)}$ shear modulus of an isotropic material in the subcell $(\alpha\beta\gamma)$

$\varepsilon^{I(\alpha\beta\gamma)}$ local inelastic strain components in the subcell $(\alpha\beta\gamma)$ (for viscoplastic materials)

$\varepsilon^{p(\alpha\beta\gamma)}$ local plastic strain components in the subcell $(\alpha\beta\gamma)$

$e_{ij(l,m,n)}^{(\alpha\beta\gamma)}$ coefficients of the total strain series expansion in the subcell $(\alpha\beta\gamma)$

$\tau_{ij(l,m,n)}^{(\alpha\beta\gamma)}$ coefficients of the stress series expansion in the subcell $(\alpha\beta\gamma)$

$\tau_{ij(l,m,n)}^{T(\alpha\beta\gamma)}$ coefficients of the thermal stress series expansion in the subcell $(\alpha\beta\gamma)$

$\sigma_{ij}^{T(\alpha\beta\gamma)}$ thermal stress components in the subcell $(\alpha\beta\gamma)$

$R_{ij(l,m,n)}^{(\alpha\beta\gamma)}$ inelastic strain distribution components in the subcell $(\alpha\beta\gamma)$

P_n Legendre polynomial of order n

$\Lambda^{(\alpha\beta\gamma)}$ inelastic flow function in the subcell $(\alpha\beta\gamma)$

$W_p^{(\alpha\beta\gamma)}$ plastic work in the subcell $(\alpha\beta\gamma)$

$Z^{(\alpha\beta\gamma)}$ state variable associated with the viscoplastic material in the subcell $(\alpha\beta\gamma)$

$\mathrm{d}\lambda^{(\alpha\beta\gamma)}$ plastic flow function increment of the material in the subcell $(\alpha\beta\gamma)$

$\boldsymbol{N}, \boldsymbol{M}$ force and moment resultant vectors

1. INTRODUCTION

Recently, a new concept has evolved for improving the performance of advanced composite materials that involves tailoring the internal microstructure or architecture of the material. This idea originated in Japan and has been explored vigorously by Japanese researchers who have coined the term "functionally gradient materials" (FGMs) to describe this newly emerging class of composites (cf. Yamanouchi *et al.*, 1990). The idea involves spatially grading the properties of the material by using variable spacings between individual inclusions, as well as by using inclusions with different properties, sizes and shapes. Such an approach offers a number of advantages over the more traditional methods of tailoring the compliance of composite materials or structural elements, and opens up new horizons for novel applications. Grading or tailoring the internal microstructure of a composite material or a structural component allows the designer to truly integrate both the material and structural considerations into the final design and final product. This brings the entire structural design process to the material level in the purest sense, thereby increasing the number of possible material configurations for specific applications.

Functionally graded composites are ideal candidates for applications involving severe thermal gradients, ranging from thermal structures in advanced aircraft and aerospace engines to circuit boards. The potential benefits that may be derived from this new class of composites have led to increased activities in the areas of processing and materials science of these materials. However, as discussed by Aboudi *et al.* (1993), these activities are seriously handicapped by the lack of appropriate computational strategies for the response of functionally graded materials that explicitly couple the heterogeneous microstructure of the material with the global analysis. The standard micromechanical approach used to analyse the response of this class of materials is to decouple the local and global effects by assuming the existence of a representative volume element (RVE) at every point within the composite (cf. Wakashima and Tsukamoto, 1990). In the presence of large material and field variable gradients, however, this assumption may lead to erroneous results (cf. Hill, 1963; Pagano, 1974). As a result of the limitation of the standard micromechanical approaches, a new micromechanical theory, that explicitly couples the local and global effects, has been developed and applied to functionally graded composites (FGCs) (Aboudi *et al.*, 1993, 1994a,b). In particular, this new higher-order theory for functionally graded materials (HOTFGM) was used to assess the limits of applicability of the standard micromechanical approach in predicting local stresses in the fiber and matrix phases of FGCs

subjected to a thermal gradient (Pindera *et al.*, 1994). It was shown that the simplified uncoupled approach is inaccurate when the dimension of the reinforcement phase is large relative to the dimension of the composite.

The original formulation of the new theory was limited to thermo-elastic analysis of FGCs involving one dimension along which both the spacings between inclusions and the applied temperature gradient vary. The properties of the individual phases remained constant with temperature. Therefore, in order to realistically model the response of FGCs with metallic matrices, the new theory is extended herein to include temperature-dependent material properties and inelastic response of the individual phases. In particular, two types of inelastic constitutive theories are employed to model the behavior of the metallic phases, namely the classical incremental plasticity and the Bodner–Partom unified viscoplasticity theory. To set the elastic results generated with the original formulation of the theory in perspective, extensive comparisons between elastic and inelastic predictions are presented for uniformly and nonuniformly spaced unidirectional SiC/Ti composites subjected to a through-the-thickness temperature gradient. The comparison includes the internal stress distributions as well as the inplane force and moment resultants required to keep a composite plate straight in the presence of a temperature gradient. The incorporation of inelastic constitutive theories which describe the response of the metallic phases enables one to identify those regions where inelastic effects cannot be disregarded, especially in the presence of high thermal and stress gradients. Thus the importance of the inelastic effects on the overall response of FGCs can now be quantitatively assessed. In addition, the theory is employed to study the potential of tailoring the microstructure of SiC particulate-reinforced metallic layers protected by a ceramic thermal barrier coating at the surface exposed to an elevated temperature. Results are compared with the response of a bi-material and tri-material plate laminated with homogeneous plies under the same thermal gradient. The comparison clearly illustrates the advantages that can be derived from the concept of internal temperature management through embedding of differently-distributed particulate inclusions in metallic layers subjected to a temperature gradient.

2. ANALYTICAL MODEL

HOTFGM is based on the geometric model of a heterogeneous composite with a finite thickness H, extending to infinity in the x_2–x_3 plane, and subjected to a temperature gradient, Fig. 1. The composite is reinforced by periodic arrays of fibers in the direction of the x_2 axis or the x_3 axis, or both. In the direction of the x_1 axis, hereafter called the functionally gradient (FG) direction, the fiber spacing between adjacent arrays may vary. The reinforcing fibers can be either continuous [Fig. 1(a)] or finite-length [Fig. 1(b)]. The heterogeneous composite is constructed using the basic building block or repeating unit cell, Fig. 2. This unit cell consists of eight subcells designated by the triplet $(\alpha\beta\gamma)$. Each index α, β, γ takes on the values 1 or 2 which indicate the relative position of the given subcell along the x_1, x_2 and x_3 axis, respectively. The dimensions of the unit cell along the x_2 and x_3 axes, h_1, h_2, and l_1, l_2, are fixed for the given configuration since these are the periodic directions, whereas the dimensions along the x_1 axis or the FG direction, $d_1^{(p)}, d_2^{(p)}$, can vary from unit cell to unit cell. The dimensions of the subcells within a given cell along the FG direction are designated with a running index p which identifies the cell number, where p remains constant in the x_2–x_3 plane. For the other two directions, x_2 and x_3, the corresponding indices q and r are introduced. Thus a given cell is designated by the triplet (p, q, r) for $p = 1, 2, \ldots, M$, where M is the number of cells in the thickness or FG direction, and an infinite range of q and r due to the periodicity of the composite in the x_2 and x_3 directions.

It is important to note that the repeating unit cell in the present framework is not taken to be an RVE whose effective properties can be obtained through local homogenization, as is done in the standard uncoupled micromechanical approaches based on the concept of *local action* (Malvern, 1969). Rather, the RVE herein comprises an entire column of such cells spanning the thickness of the plate. Thus the principle of local action is not applicable at the individual cell level, requiring the response of each cell to be explicitly coupled to the

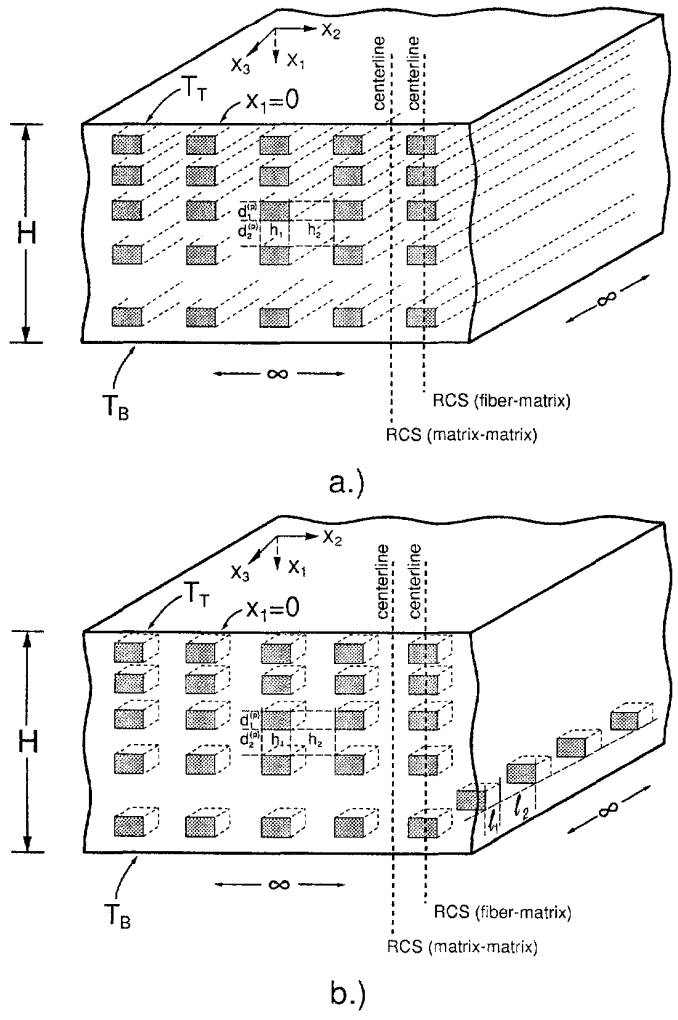

Fig. 1. Composite with nonperiodic fiber distribution in the x_1 direction: (a) unidirectionally reinforced material; (b) particulate inclusion-reinforced material. RCS denotes the representative cross-section.

response of the entire column of cells in the FG direction. This is what is meant by the statement that the present approach explicitly couples the microstructural details with the global analysis, and thus sets HOTFGM apart from the standard approaches found in the literature.

2.1. *Outline of the solution technique*

The solution of the thermo-mechanical boundary-value problem outlined in the foregoing in the presence of inelastic and temperature-dependent effects is solved in two steps, following the general framework for the solution of the corresponding thermo-elastic problem discussed previously (Aboudi *et al.*, 1993). In the first step, the temperature distribution in a single column of cells, representative of the composite-at-large, spanning the FG dimension is determined by solving the heat equation under steady-state conditions in each cell subject to the appropriate continuity and compatibility conditions. These conditions ensure that the given cell is indistinguishable from the adjacent cells in the x_2–x_3 plane. The solution to the heat equation is obtained by approximating the temperature field in each subcell of a repeating unit cell using a quadratic expansion in the local coordinates $\bar{\mathbf{x}}^{(\alpha)}$, $\bar{\mathbf{x}}^{(\beta)}$, $\bar{\mathbf{x}}^{(\gamma)}$ centered at the subcell's mid-point. A higher-order representation of the temperature field is necessary in order to capture the local effects created by the

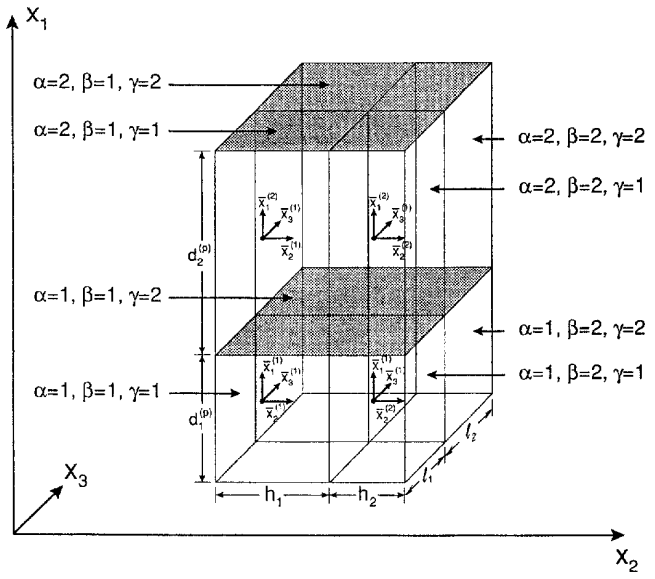

Fig. 2. The repeating unit cell of a composite with nonperiodic fiber distribution in the x_1 direction.

thermal gradient, the microstructure of the composite and the finite dimension in the FG direction, in contrast with previous treatments involving fully periodic composite media. The unknown coefficients associated with each term in the expansion are then obtained by constructing a system of equations that satisfies the requirements of a standard boundary-value problem for the given temperature field approximation. That is, the heat equation is satisfied in a volumetric sense, and the thermal and heat flux continuity conditions within a given cell, as well as between a given cell and adjacent cells, are imposed in an average sense.

Given the temperature distribution in a single column of cells representative of the composite-at-large, internal displacements, strains and stresses are subsequently generated by solving the equilibrium equations in each cell subject to appropriate continuity and boundary conditions. The solution is obtained by approximating the displacement field in the FG direction in each subcell using a quadratic expansion in local coordinates within the subcell. The displacement field in the x_2 and x_3 directions, on the other hand, is approximated using linear expansion in local coordinates to reflect the periodic character of the composite's microstructure in the x_2–x_3 plane. The unknown coefficients associated with each term in the expansion are obtained by satisfying the appropriate field equations in a volumetric sense, together with the boundary conditions and continuity of displacements and tractions between individual subcells of a given cell, and between adjacent cells. The continuity conditions are imposed in an average sense. This results in a coupled system of equations involving the unknown coefficients in the displacement representation for each cell. The presence of temperature-dependent and inelastic effects requires an incremental solution technique of these equations at each step of applied loading since integrals of plastic strain distributions, which depend implicitly on the unknown coefficients, appear in the system of equations.

An outline of the governing equations for the temperature and displacement fields in the individual subcells within the column of cells considered in solving the outlined boundary-value problem is given in the sequel. A detailed derivation of these equations has been presented in Appendices A and B in Aboudi *et al.* (1994b), and thus will not be repeated here so as not to obscure the basic concepts by the involved algebraic manipulations.

2.2. *Thermal analysis*

Suppose that the composite material occupies the region $0 \leqslant x_1 \leqslant H$, $|x_2| < \infty$, $|x_3| < \infty$. Let M denote the number of cells in the interval $0 \leqslant x_1 \leqslant H$, where $H = \Sigma$

$(d_1^{(p)}+d_2^{(p)})$, $p=1,\ldots,M$. For $p=2,\ldots,M-1$ the cells are internal, whereas for $p=1$ and $p=M$ they are boundary cells. The triplet (p,q,r) used to identify the pth cell is implicitly assumed to be attached to the field variables associated with this cell, and thus is not explicitly displayed for notational simplicity.

Let the composite be subjected to the temperature T_T on the top surface ($x_1=0$) and to T_B on the bottom surface ($x_1=H$). For a steady-state situation, the heat flux field in the material occupying the subcell $(\alpha\beta\gamma)$ in the region defined by $|\bar{x}_1^{(\alpha)}|\leqslant d_\alpha^{(p)}/2$, $|\bar{x}_2^{(\beta)}|\leqslant h_\beta/2$, $|\bar{x}_3^{(\gamma)}|\leqslant l_\gamma/2$ of the pth cell must satisfy the equation:

$$\partial_1 q_1^{(\alpha\beta\gamma)}+\partial_2 q_2^{(\alpha\beta\gamma)}+\partial_3 q_3^{(\alpha\beta\gamma)}=0 \tag{1}$$

where $\partial_1=\partial/\partial\bar{x}_1^{(\alpha)}$, $\partial_2=\partial/\partial\bar{x}_2^{(\beta)}$, $\partial_3=\partial/\partial\bar{x}_3^{(\gamma)}$. The components of the heat flux vector $q_i^{(\alpha\beta\gamma)}$ in this subcell are derived from the temperature field as follows:

$$q_i^{(\alpha\beta\gamma)}=-k_i^{(\alpha\beta\gamma)}\partial_i T^{(\alpha\beta\gamma)},\ (i=1,2,3\,;\text{no sum}) \tag{2}$$

where $k_i^{(\alpha\beta\gamma)}$ are the coefficients of heat conductivity of the material occupying the subcell $(\alpha\beta\gamma)$, and no summation is implied by repeated Greek letters in the above and henceforth.

The temperature distribution $T^{(\alpha\beta\gamma)}$ in the subcell $(\alpha\beta\gamma)$ of the pth cell is approximated by a second order expansion in the local coordinates $\bar{x}_1^{(\alpha)}$, $\bar{x}_2^{(\beta)}$, and $\bar{x}_3^{(\gamma)}$ as follows:

$$T^{(\alpha\beta\gamma)}=T_0^{(\alpha\beta\gamma)}+\bar{x}_1^{(\alpha)}T_1^{(\alpha\beta\gamma)}+\tfrac{1}{2}\left(3\bar{x}_1^{(\alpha)2}-\frac{d_\alpha^{(p)2}}{4}\right)T_2^{(\alpha\beta\gamma)}+\tfrac{1}{2}\left(3\bar{x}_2^{(\beta)2}-\frac{h_\beta^2}{4}\right)T_3^{(\alpha\beta\gamma)}+\tfrac{1}{2}\left(3\bar{x}_3^{(\gamma)2}-\frac{l_\gamma^2}{4}\right)T_4^{(\alpha\beta\gamma)} \tag{3}$$

where $T_0^{(\alpha\beta\gamma)}$, which is the temperature at the center of the subcell, and $T_i^{(\alpha\beta\gamma)}$ $(i=1,\ldots,4)$ are unknown coefficients which are determined from conditions that will be outlined subsequently.

Given the five unknown quantities $(T_0^{(\alpha\beta\gamma)},\ldots,T_4^{(\alpha\beta\gamma)})$ associated with each subcell, and eight subcells within each unit cell, $40M$ unknown quantities must be determined for a composite with M rows of cells in the FG direction. These unknown quantities are determined by first satisfying the heat conduction equation, as well as the first and second moments of this equation in each subcell. This is carried out in a volumetric sense for each subcell in view of the temperature field approximation given by eqn (3). For this reason the first and second moments must be considered. Subsequently, continuity of heat flux and temperature is imposed in an average sense at the interfaces separating adjacent subcells, as well as neighboring cells. Fulfilment of these field equations and continuity conditions, in conjunction with the imposed thermal boundary conditions at the top and bottom surfaces of the composite, provides the necessary $40M$ equations given below for the $40M$ unknown coefficients in the temperature field expansion. Details of the derivation of these equations have been provided by Aboudi *et al.* (1993, 1994b).

Relations arising from the heat conduction equation (for p = 1, 2, . . . , M).

$$k_1^{(\alpha\beta\gamma)}T_2^{(\alpha\beta\gamma)}+k_2^{(\alpha\beta\gamma)}T_3^{(\alpha\beta\gamma)}+k_3^{(\alpha\beta\gamma)}T_4^{(\alpha\beta\gamma)}=0. \tag{4}$$

Relations arising from the heat flux continuity requirements. Between individual subcells (for $p=1,2,\ldots,M$)

$$h_1 k_2^{(\alpha 1\gamma)}T_3^{(\alpha 1\gamma)}+h_2 k_2^{(\alpha 2\gamma)}T_3^{(\alpha 2\gamma)}=0 \tag{5}$$

$$l_1 k_3^{(\alpha\beta 1)}T_4^{(\alpha\beta 1)}+l_2 k_3^{(\alpha\beta 2)}T_4^{(\alpha\beta 2)}=0 \tag{6}$$

Between neighboring cells (for $p=2,\ldots,M$)

$$3k_2^{(1\beta\gamma)}T_3^{(1\beta\gamma)}+3k_3^{(1\beta\gamma)}T_4^{(1\beta\gamma)}+\frac{3}{2}\frac{d_2^{(p)}}{d_1^{(p)}}[k_2^{(2\beta\gamma)}T_3^{(2\beta\gamma)}+k_3^{(2\beta\gamma)}T_4^{(2\beta\gamma)}]+$$

$$\frac{3}{2}\frac{d_2^{(p-1)}}{d_1^{(p)}}[k_2^{(2\beta\gamma)}T_3^{(2\beta\gamma)}+k_3^{(2\beta\gamma)}T_4^{(2\beta\gamma)}]^{(p-1,q,r)}+\frac{1}{d_1^{(p)}}[k_1^{(2\beta\gamma)}T_1^{(2\beta\gamma)}-k_1^{(2\beta\gamma)}T_1^{(2\beta\gamma)}|^{(p-1,q,r)}]=0 \quad (7)$$

$$k_1^{(1\beta\gamma)}T_1^{(1\beta\gamma)}=\tfrac{1}{2}k_1^{(2\beta\gamma)}T_1^{(2\beta\gamma)}+\tfrac{1}{2}k_1^{(2\beta\gamma)}T_1^{(2\beta\gamma)}|^{(p-1,q,r)}+\tfrac{3}{4}d_2^{(p)}[k_2^{(2\beta\gamma)}T_3^{(2\beta\gamma)}+k_3^{(2\beta\gamma)}T_4^{(2\beta\gamma)}]-$$

$$\tfrac{3}{4}d_2^{(p-1)}[k_2^{(2\beta\gamma)}T_3^{(2\beta\gamma)}+k_3^{(2\beta\gamma)}T_4^{(2\beta\gamma)}]^{(p-1,q,r)}. \quad (8)$$

Relations arising from the thermal continuity requirements. Between individual subcells (for $p = 1, 2, \ldots, M$)

$$T_0^{(1\beta\gamma)}+\tfrac{1}{2}d_1^{(p)}T_1^{(1\beta\gamma)}+\tfrac{1}{4}d_1^{(p)2}T_2^{(1\beta\gamma)}=T_0^{(2\beta\gamma)}-\tfrac{1}{2}d_2^{(p)}T_1^{(2\beta\gamma)}+\tfrac{1}{4}d_2^{(p)2}T_2^{(2\beta\gamma)} \quad (9)$$

$$T_0^{(\alpha1\gamma)}+\tfrac{1}{4}h_1^2T_3^{(\alpha1\gamma)}=T_0^{(\alpha2\gamma)}+\tfrac{1}{4}h_2^2T_3^{(\alpha2\gamma)} \quad (10)$$

$$T_0^{(\alpha\beta1)}+\tfrac{1}{4}l_1^2T_4^{(\alpha\beta1)}=T_0^{(\alpha\beta2)}+\tfrac{1}{4}l_2^2\,T_4^{(\alpha\beta2)}. \quad (11)$$

Between neighboring cells (for $p = 1, 2, \ldots, M-1$)

$$[T_0^{(1\beta\gamma)}-\tfrac{1}{2}d_1^{(p+1)}T_1^{(1\beta\gamma)}+\tfrac{1}{4}d_1^{(p+1)2}T_2^{(1\beta\gamma)}]^{(p+1,q,r)}=T_0^{(2\beta\gamma)}+\tfrac{1}{2}d_2^{(p)}T_1^{(2\beta\gamma)}+\tfrac{1}{4}d_2^{(p)2}T_2^{(2\beta\gamma)}. \quad (12)$$

We note that the continuity of temperature between neighboring cells in the x_2 and x_3-directions is automatically satisfied by the chosen temperature field representation which reflects the periodic character of the composite in these directions.

Boundary conditions.

Top ($p = 1$)

$$T^{(1\beta\gamma)}=T_{\mathrm{T}},\ \bar{x}_1^{(1)}=-\tfrac{1}{2}d_1^{(1)} \quad (13)$$

Bottom ($p = M$)

$$T^{(2\beta\gamma)}=T_{\mathrm{B}},\ \bar{x}_1^{(2)}=\tfrac{1}{2}d_2^{(M)} \quad (14)$$

where T_{T} and T_{B} are the applied temperatures at the top and bottom surface of the composite plate.

The governing equations at the interior and boundary cells form a system of $40M$ linear algebraic equations in the unknown coefficients $T_i^{(\alpha\beta\gamma)|p}$ ($i = 0, \ldots, 4$; $\alpha, \beta, \gamma = 1,2$; $p = 1, \ldots, M$). Their solution determines the temperature distribution within the FG composite subjected to the boundary conditions given in eqns (13) and (14). The final form of this system of equations is symbolically represented below

$$\boldsymbol{\kappa}\mathbf{T}=\mathbf{t} \quad (15)$$

where the structural thermal conductivity matrix $\boldsymbol{\kappa}$ contains information on the geometry and thermal conductivities of the individual subcells ($\alpha\beta\gamma$) in the M cells spanning the thickness of the FG plate, the thermal coefficient vector $\mathbf{T} = (\mathbf{T}_1^{(111)}, \ldots, \mathbf{T}_M^{(222)})$, where $\mathbf{T}_p^{(\alpha\beta\gamma)} = (T_0, T_1, T_2, T_3, T_4)_p^{(\alpha\beta\gamma)}$, contains the unknown coefficients that describe the thermal field in each subcell, and the thermal force vector $\mathbf{t} = (T_{\mathrm{T}}, 0, \ldots, 0, T_{\mathrm{B}})$ contains information on the thermal boundary conditions.

2.3. *Mechanical analysis: problem formulation*

Given the temperature distribution generated by the applied surface temperatures T_T and T_B obtained in the preceding section, we now proceed to determine the resulting displacement and stress fields. This is carried out for uniform normal (i.e. no shearing) mechanical loading applied to the surfaces of the composite.

2.3.1. *Equations of equilibrium.* The stress field in the subcell $(\alpha\beta\gamma)$ of the pth cell generated by the given temperature field must satisfy the equilibrium equations

$$\partial_1 \sigma_{1j}^{(\alpha\beta\gamma)} + \partial_2 \sigma_{2j}^{(\alpha\beta\gamma)} + \partial_3 \sigma_{3j}^{(\alpha\beta\gamma)} = 0, \quad j = 1,2,3 \tag{16}$$

where the operator ∂_i has been defined previously. The components of the stress tensor, assuming that the material occupying the subcell $(\alpha\beta\gamma)$ of the pth cell is orthotropic, are related to the strain components through the familiar generalized Hooke's law

$$\sigma_{ij}^{(\alpha\beta\gamma)} = c_{ijkl}^{(\alpha\beta\gamma)}(\varepsilon_{kl}^{(\alpha\beta\gamma)} - \varepsilon_{kl}^{I(\alpha\beta\gamma)}) - \Gamma_{ij}^{(\alpha\beta\gamma)} T^{(\alpha\beta\gamma)} \tag{17}$$

where $c_{ijkl}^{(\alpha\beta\gamma)}$ are the elements of the stiffness tensor, $\varepsilon_{ij}^{I(\alpha\beta\gamma)}$ are the inelastic strain components, and the elements $\Gamma_{ij}^{(\alpha\beta\gamma)}$ of the so-called thermal tensor are the products of the stiffness tensor and the thermal expansion coefficients. In this paper, we consider elastic orthotropic materials or inelastic isotropic materials. Hence, eqn (17) reduces to

$$\sigma_{ij}^{(\alpha\beta\gamma)} = c_{ijkl}^{(\alpha\beta\gamma)} \varepsilon_{kl}^{(\alpha\beta\gamma)} - 2\mu_{(\alpha\beta\gamma)} \varepsilon_{ij}^{I(\alpha\beta\gamma)} - \sigma_{ij}^{T(\alpha\beta\gamma)} \tag{18}$$

where $\mu_{(\alpha\beta\gamma)}$ is the elastic shear modulus of the material filling the given subcell $(\alpha\beta\gamma)$, and the term $\sigma_{ij}^{T(\alpha\beta\gamma)}$, henceforth referred to as thermal stress, stands for the thermal contribution $\Gamma_{ij}^{(\alpha\beta\gamma)} T^{(\alpha\beta\gamma)}$. The components of the strain tensor in the individual subcells are, in turn, obtained from the strain–displacement relations

$$\varepsilon_{ij}^{(\alpha\beta\gamma)} = \tfrac{1}{2}(\partial_i u_j^{(\alpha\beta\gamma)} + \partial_j u_i^{(\alpha\beta\gamma)}), \quad i,j = 1,2,3. \tag{19}$$

Given the relation between the stresses and displacement gradients obtained from eqns (18) and (19), a displacement field is sought that satisfies the three equilibrium equations together with the continuity and boundary conditions that follow.

2.3.2. *Traction continuity conditions.* The continuity of tractions at the interfaces separating adjacent subcells within the repeating unit cell (p,q,r) is fulfilled by requiring that

$$\sigma_{1i}^{(1\beta\gamma)}\big|_{x_1^{(1)} = d_1^{(p)}/2}^{(p,q,r)} = \sigma_{1i}^{(2\beta\gamma)}\big|_{x_1^{(2)} = -d_2^{(p)}/2}^{(p,q,r)} \tag{20a}$$

$$\sigma_{2i}^{(\alpha 1\gamma)}\big|_{x_2^{(1)} = h_1/2}^{(p,q,r)} = \sigma_{2i}^{(\alpha 2\gamma)}\big|_{x_2^{(2)} = -h_2/2}^{(p,q,r)} \tag{20b}$$

$$\sigma_{3i}^{(\alpha\beta 1)}\big|_{x_3^{(1)} = l_1/2}^{(p,q,r)} = \sigma_{3i}^{(\alpha\beta 2)}\big|_{x_3^{(2)} = -l_2/2}^{(p,q,r)}. \tag{20c}$$

In addition to the above continuity conditions within the pth cell, the traction continuity at the interfaces between neighboring cells must be ensured. These conditions are fulfilled by requiring that

$$\sigma_{1i}^{(1\beta\gamma)}\big|_{x_1^{(1)} = -d_1^{(p+1)}/2}^{(p+1,q,r)} = \sigma_{1i}^{(2\beta\gamma)}\big|_{x_1^{(2)} = d_2^{(p)}/2}^{(p,q,r)} \tag{21a}$$

$$\sigma_{2i}^{(\alpha 1\gamma)}\big|_{x_2^{(1)} = -h_1/2}^{(p,q+1,r)} = \sigma_{2i}^{(\alpha 2\gamma)}\big|_{x_2^{(2)} = h_2/2}^{(p,q,r)} \tag{21b}$$

$$\sigma_{3i}^{(\alpha\beta 1)}\big|_{x_3^{(1)} = -l_1/2}^{(p,q,r+1)} = \sigma_{3i}^{(\alpha\beta 2)}\big|_{x_3^{(2)} = l_2/2}^{(p,q,r)}. \tag{21c}$$

2.2.3. *Displacement continuity conditions.* At the interfaces of the subcells within the repeating unit cell (p, q, r) the displacements $\mathbf{u} = (u_1, u_2, u_3)$ must be continuous

$$\mathbf{u}^{(1\beta\gamma)}\big|^{(p,q,r)}_{\bar{x}_2^{(1)}=d_1^{(p)}/2} = \mathbf{u}^{(2\beta\gamma)}\big|^{(p,q,r)}_{\bar{x}_1^{(2)}=-d_1^{(p)}/2} \tag{22a}$$

$$\mathbf{u}^{(\alpha 1\gamma)}\big|^{(p,q,r)}_{\bar{x}_2^{(1)}=h_1/2} = \mathbf{u}^{(\alpha 2\gamma)}\big|^{(p,q,r)}_{\bar{x}_2^{(2)}=-h_2/2} \tag{22b}$$

$$\mathbf{u}^{(\alpha\beta 1)}\big|^{(p,q,r)}_{\bar{x}_3^{(1)}=l_1/2} = \mathbf{u}^{(\alpha\beta 2)}\big|^{(p,q,r)}_{\bar{x}_3^{(2)}=-l_2/2} \tag{22c}$$

while the continuity of displacements between neighboring cells is ensured by requiring that

$$\mathbf{u}^{(1\beta\gamma)}\big|^{(p+1,q,r)}_{\bar{x}_1^{(1)}=-d_1^{(p+1)}/2} = \mathbf{u}^{(2\beta\gamma)}\big|^{(p,q,r)}_{\bar{x}_1^{(2)}=d_2^{(p)}/2} \tag{23a}$$

$$\mathbf{u}^{(\alpha 1\gamma)}\big|^{(p,q+1,r)}_{\bar{x}_2^{(1)}=-h_1/2} = \mathbf{u}^{(\alpha 2\gamma)}\big|^{(p,q,r)}_{\bar{x}_2^{(2)}=h_2/2} \tag{23b}$$

$$\mathbf{u}^{(\alpha\beta 1)}\big|^{(p,q,r+1)}_{\bar{x}_3^{(1)}=-l_1/2} = \mathbf{u}^{(\alpha\beta 2)}\big|^{(p,q,r)}_{\bar{x}_3^{(2)}=l_2/2}. \tag{23c}$$

2.3.4. *Boundary conditions.* The final set of conditions that the solution for the displacement field must satisfy are the boundary conditions at the top and bottom surfaces. The normal stress in the cell $p = 1$ at the top surface must equal the applied normal stress $f(t)$

$$\sigma_1^{(1\beta\gamma)}\big|^{(1,q,r)} = f(t), \quad \bar{x}_1^{(1)} = -\tfrac{1}{2}d_1^{(1)} \tag{24}$$

with $f(t)$ describing the temporal variation of this loading, whereas in the cell $p = M$ at the bottom surface the condition that the surface $x_1 = H$ is rigidly clamped (say) is imposed

$$u_1^{(2\beta\gamma)}\big|^{(M,q,r)} = 0, \quad \bar{x}_1^{(2)} = \tfrac{1}{2}d_2^{(M)}. \tag{25}$$

For other types of boundary conditions, eqns (24)–(25) should be modified accordingly. It should be noted that in the majority of composite applications of technological interest, $f(t)$ in eqn (24) will likely be zero since, in general, thin laminated composites are designed to support loads in the lamination plane rather than in the out-of-plane direction. However, modeling of processing of functionally graded composites will typically involve application of transverse loads which, together with the applied thermal loads during fabrication cooldown, will induce residual stresses. The proposed theory is sufficiently general to model such combined thermo-mechanical loading histories. In this paper, however, we neglect residual stresses induced during fabrication. This issue will be considered elsewhere.

2.4. *Mechanical analysis: solution*

Due to symmetry considerations, the displacement field in the subcell $(\alpha\beta\gamma)$ of the pth cell is approximated by a second-order expansion in the local coordinates $\bar{x}_1^{(\alpha)}$, $\bar{x}_2^{(\beta)}$, and $\bar{x}_3^{(\gamma)}$ as follows:

$$u_1^{(\alpha\beta\gamma)} = w_1^{(\alpha\beta\gamma)} + \bar{x}_1^{(\alpha)}\phi_1^{(\alpha\beta\gamma)} + \tfrac{1}{2}(3\bar{x}_1^{(\alpha)2} - \tfrac{1}{4}d_\alpha^{(p)2})U_1^{(\alpha\beta\gamma)} + \tfrac{1}{2}(3\bar{x}_2^{(\beta)2} - \tfrac{1}{4}h_\beta^2)V_1^{(\alpha\beta\gamma)} + \tfrac{1}{2}(3\bar{x}_3^{(\gamma)2} - \tfrac{1}{4}l_\gamma^2)W_1^{(\alpha\beta\gamma)}$$

$$u_2^{(\alpha\beta\gamma)} = \bar{x}_2^{(\beta)}\chi_2^{(\alpha\beta\gamma)}$$

$$u_3^{(\alpha\beta\gamma)} = \bar{x}_3^{(\gamma)}\psi_3^{(\alpha\beta\gamma)} \tag{26}$$

where $w_1^{(\alpha\beta\gamma)}$, which are the displacements at the center of the subcell, and $U_1^{(\alpha\beta\gamma)}$, $V_1^{(\alpha\beta\gamma)}$, $W_1^{(\alpha\beta\gamma)}$, $\phi_1^{(\alpha\beta\gamma)}$, $\chi_2^{(\alpha\beta\gamma)}$, and $\psi_3^{(\alpha\beta\gamma)}$ must be determined from conditions similar to those employed in the thermal problem. In this case, there are $56M$ unknown quantities. The determination of these quantities parallels that of the thermal problem. Here, the heat

conduction equation is replaced by the three equilibrium equations, and the continuity of tractions and displacements at the various interfaces replaces the continuity of heat fluxes and temperature. Finally, the boundary conditions involve the appropriate mechanical quantities.

An explicit derivation of the system of linear algebraic equations for the unknown microvariables appearing in the displacement field expansion has been provided by Aboudi *et al.* (1993) when the individual phases are linearly elastic. In this case, the unknown microvariables depend explicitly on the internal temperature field, internal distribution and geometry of the individual constituents and their properties. The chosen representation of the displacement field immediately results in a unique form of the stress field generated from the assumed displacements using strain–displacement and constitutive relations. *In the inelastic problem however, the displacement field microvariables depend implicitly on the inelastic strain distributions, giving rise to a higher-order stress field than the strain field generated from the assumed displacement field representation.* In other words, the distribution of the local stresses within each subcell will be much more complicated than the linear strain field arising from the assumed displacement field. Herein, we represent this higher-order stress field in the presence of inelastic effects using a higher-order Legendre polynomial expansion in the local coordinates. In view of this, the strain field generated from the assumed displacement field, together with the resulting mechanical and thermal stress fields, are expressed in terms of Legendre polynomials as follows

$$\varepsilon_{ij}^{(\alpha\beta\gamma)} = \sum_{l=0}^{\infty}\sum_{m=0}^{\infty}\sum_{n=0}^{\infty}\sqrt{(1+2l)(1+2m)(1+2n)}\, e_{ij(l,m,n)}^{(\alpha\beta\gamma)} P_l(\zeta_1^{(\alpha)})P_m(\zeta_2^{(\beta)})P_n(\zeta_3^{(\gamma)}) \tag{27}$$

$$\sigma_{ij}^{(\alpha\beta\gamma)} = \sum_{l=0}^{\infty}\sum_{m=0}^{\infty}\sum_{n=0}^{\infty}\sqrt{(1+2l)(1+2m)(1+2n)}\, \tau_{ij(l,m,n)}^{(\alpha\beta\gamma)} P_l(\zeta_1^{(\alpha)})P_m(\zeta_2^{(\beta)})P_n(\zeta_3^{(\gamma)}) \tag{28}$$

$$\sigma_{ij}^{T(\alpha\beta\gamma)} = \sum_{l=0}^{\infty}\sum_{m=0}^{\infty}\sum_{n=0}^{\infty}\sqrt{(1+2l)(1+2m)(1+2n)}\, \tau_{ij(l,m,n)}^{T(\alpha\beta\gamma)} P_l(\zeta_1^{(\alpha)})P_m(\zeta_2^{(\beta)})P_n(\zeta_3^{(\gamma)}) \tag{29}$$

where the non-dimensionalized variables ζ_is, defined in the interval $-1 \leqslant \zeta_i \leqslant 1$, are expressed in terms of the local subcell coordinates as follows: $\zeta_1^{(\alpha)} = \bar{x}_1^{(\alpha)}/(d_\alpha^{(p)}/2)$, $\zeta_2^{(\beta)} = \bar{x}_2^{(\beta)}/(h_\beta/2)$, and $\zeta_3^{(\gamma)} = \bar{x}_3^{(\gamma)}/(l_\gamma/2)$.

For the given displacement field representation, eqn (26), the upper limits on the summations in eqn (27) become 1, while for the given temperature distribution, eqn (3), the upper limits on the summations in eqn (29) become 2. The coefficients $e_{ij(l,m,n)}^{(\alpha\beta\gamma)}$, $\tau_{ij(l,m,n)}^{(\alpha\beta\gamma)}$, $\tau_{ij(l,m,n)}^{T(\alpha\beta\gamma)}$ in the above expansions are determined as follows.

The strain coefficients $e_{ij(l,m,n)}^{(\alpha\beta\gamma)}$ are explicitly determined in terms of the displacement field microvariables of eqn (26) using orthogonal properties of Legendre polynomials. For example

$$e_{11(0,0,0)}^{(\alpha\beta\gamma)} = \phi_1^{(\alpha\beta\gamma)}. \tag{30}$$

The complete set of non-zero strain coefficients $e_{ij(l,m,n)}^{(\alpha\beta\gamma)}$ is given in the Appendix.

The stress coefficients $\tau_{ij(l,m,n)}^{(\alpha\beta\gamma)}$ are expressed in terms of the strain coefficients, the thermal stress coefficients and the unknown inelastic strain distributions by first substituting the Legendre polynomial representations for $\boldsymbol{\varepsilon}^{(\alpha\beta\gamma)}$, $\boldsymbol{\sigma}^{(\alpha\beta\gamma)}$ and $\boldsymbol{\sigma}^{T(\alpha\beta\gamma)}$ into the constitutive eqns (18), and then utilizing the orthogonality of Legendre polynomials

$$\tau_{ij(l,m,n)}^{(\alpha\beta\gamma)} = c_{ijkl}^{(\alpha\beta\gamma)} e_{kl(l,m,n)}^{(\alpha\beta\gamma)} - \tau_{ij(l,m,n)}^{T(\alpha\beta\gamma)} - R_{ij(l,m,n)}^{(\alpha\beta\gamma)}. \tag{31}$$

The thermal stress coefficients $\tau_{ij(l,m,n)}^{T(\alpha\beta\gamma)}$ can be similarly expressed in terms of the temperature field microvariables $T_i^{T(\alpha\beta\gamma)}$ of eqn (3). For example

$$\tau_{11(0,0,0)}^{T(\alpha\beta\gamma)} = \Gamma_{11}^{(\alpha\beta\gamma)} T_0^{(\alpha\beta\gamma)}. \tag{32}$$

The complete set of non-zero thermal stress coefficients $\tau_{ij(l,m,n)}^{T(\alpha\beta\gamma)}$ is given in the Appendix.

The $R_{ij(l,m,n)}^{(\alpha\beta\gamma)}$ terms represent inelastic strain distributions calculated in the following manner

$$R_{ij(l,m,n)}^{(\alpha\beta\gamma)} = \mu_{(\alpha\beta\gamma)} \frac{\sqrt{(1+2l)(1+2m)(1+2n)}}{4} \times \int_{-1}^{1}\int_{-1}^{1}\int_{-1}^{1} \varepsilon_{ij}^{I(\alpha\beta\gamma)} P_l(\zeta_1^{(\alpha)}) P_m(\zeta_2^{(\beta)}) P_n(\zeta_3^{(\gamma)}) \, \mathrm{d}\zeta_1^{(\alpha)} \, \mathrm{d}\zeta_2^{(\beta)} \, \mathrm{d}\zeta_3^{(\gamma)}. \tag{33}$$

It should be noted that the choice of the Legendre polynomials in the above expansions is motivated by the simplicity of their orthogonal properties (i.e. the weight function is equal to one). It is possible, of course, to use any other orthogonal set of polynomials.

2.4.1. *Equations of equilibrium.* In the course of satisfying the equilibrium equations in a volumetric sense, it is convenient to define the following stress quantities

$$S_{ij(l,m,n)}^{(\alpha\beta\gamma)} = \frac{1}{v_{(\alpha\beta\gamma)}^{(p)}} \int_{-d_\alpha^{(p)}/2}^{d_\alpha^{(p)}/2} \int_{-h_\beta/2}^{h_\beta/2} \int_{-l_\gamma/2}^{l_\gamma/2} (\bar{x}_1^{(\alpha)})^l (\bar{x}_2^{(\beta)})^m (\bar{x}_3^{(\gamma)})^n \sigma_{ij}^{(\alpha\beta\gamma)} \, \mathrm{d}\bar{x}_1^{(\alpha)} \, \mathrm{d}\bar{x}_2^{(\beta)} \, \mathrm{d}\bar{x}_3^{(\gamma)} \tag{34}$$

where $i,j = 1,2,3$, and $v_{(\alpha\beta\gamma)}^{(p)} = d_\alpha^{(p)} h_\beta l_\gamma$ (see Fig. 1). For $l = m = n = 0$, eqn (34) provides average stresses in the subcell, whereas for other values of (l, m, n) higher-order stresses are obtained which are needed to describe the governing field equations of the higher-order continuum. These stress quantities can be evaluated explicitly in terms of the unknown coefficients $U_1^{(\alpha\beta\gamma)}, \ldots, \phi_1^{(\alpha\beta\gamma)}, \ldots, \psi_3^{(\alpha\beta\gamma)}$ by performing the required volume integration using eqns (18), (19) and (26) in eqn (34). This yields the following non-vanishing zeroth-order and first-order stress components in terms of the unknown coefficients in the displacement field expansion:

$$S_{11(0,0,0)}^{(\alpha\beta\gamma)} = c_{11}^{(\alpha\beta\gamma)} \phi_1^{(\alpha\beta\gamma)} + c_{12}^{(\alpha\beta\gamma)} \chi_2^{(\alpha\beta\gamma)} + c_{13}^{(\alpha\beta\gamma)} \psi_3^{(\alpha\beta\gamma)} - \Gamma_{11}^{(\alpha\beta\gamma)} T_0^{(\alpha\beta\gamma)} - R_{11(0,0,0)}^{(\alpha\beta\gamma)} \tag{35}$$

$$S_{22(0,0,0)}^{(\alpha\beta\gamma)} = c_{12}^{(\alpha\beta\gamma)} \phi_1^{(\alpha\beta\gamma)} + c_{22}^{(\alpha\beta\gamma)} \chi_2^{(\alpha\beta\gamma)} + c_{23}^{(\alpha\beta\gamma)} \psi_3^{(\alpha\beta\gamma)} - \Gamma_{22}^{(\alpha\beta\gamma)} T_0^{(\alpha\beta\gamma)} - R_{22(0,0,0)}^{(\alpha\beta\gamma)} \tag{36}$$

$$S_{33(0,0,0)}^{(\alpha\beta\gamma)} = c_{13}^{(\alpha\beta\gamma)} \phi_1^{(\alpha\beta\gamma)} + c_{23}^{(\alpha\beta\gamma)} \chi_2^{(\alpha\beta\gamma)} + c_{33}^{(\alpha\beta\gamma)} \psi_3^{(\alpha\beta\gamma)} - \Gamma_{33}^{(\alpha\beta\gamma)} T_0^{(\alpha\beta\gamma)} - R_{33(0,0,0)}^{(\alpha\beta\gamma)} \tag{37}$$

$$S_{11(1,0,0)}^{(\alpha\beta\gamma)} = \tfrac{1}{4} c_{11}^{(\alpha\beta\gamma)} d_\alpha^{(p)2} U_1^{(\alpha\beta\gamma)} - \tfrac{1}{12} d_\alpha^{(p)2} \Gamma_{11}^{(\alpha\beta\gamma)} T_1^{(\alpha\beta\gamma)} - \frac{d_\alpha^{(p)}}{2\sqrt{3}} R_{11(1,0,0)}^{(\alpha\beta\gamma)} \tag{38}$$

$$S_{12(0,1,0)}^{(\alpha\beta\gamma)} = \tfrac{1}{4} c_{44}^{(\alpha\beta\gamma)} h_\beta^2 V_1^{(\alpha\beta\gamma)} - \frac{h_\beta}{2\sqrt{3}} R_{12(0,1,0)}^{(\alpha\beta\gamma)} \tag{39}$$

$$S_{13(0,0,1)}^{(\alpha\beta\gamma)} = \tfrac{1}{4} c_{55}^{(\alpha\beta\gamma)} l_\gamma^2 W_1^{(\alpha\beta\gamma)} - \frac{l_\gamma}{2\sqrt{3}} R_{13(0,0,1)}^{(\alpha\beta\gamma)}. \tag{40}$$

Satisfaction of the equilibrium equations results in the following eight relations among the volume-averaged first-order stresses $S_{ij(l,m,n)}^{(\alpha\beta\gamma)}$ in the different subcells $(\alpha\beta\gamma)$ of the pth cell, after lengthy algebraic manipulations (see section 3 of Appendix B in Aboudi *et al.*, 1994b)

$$[S_{11(1,0,0)}^{(\alpha\beta\gamma)}/d_\alpha^{(p)2} + S_{12(0,1,0)}^{(\alpha\beta\gamma)}/h_\beta^2 + S_{13(0,0,1)}^{(\alpha\beta\gamma)}/l_\gamma^2]^{(p)} = 0 \tag{41}$$

where the triplet $(\alpha\beta\gamma)$ assumes all permutations of the integers 1 and 2.

2.4.2. *Traction continuity equations.* The continuity of tractions at the subcell interfaces, as well as between individual cells, associated with the x_1 (FG) direction, eqns (20a) and (21a) imposed in an average sense, is ensured by the following relations

$$[12S^{(1\beta\gamma)}_{12(0,1,0)}/h_\beta^2 + 12S^{(1\beta\gamma)}_{13(0,0,1)}/l_\gamma^2]^{(p)} + 6\frac{d_2^{(p)}}{d_1^{(p)}}[S^{(2\beta\gamma)}_{12(0,1,0)}/h_\beta^2 + S^{(2\beta\gamma)}_{13(0,0,1)}/l_\gamma^2]^{(p)} +$$

$$6\frac{d_2^{(p-1)}}{d_1^{(p)}}[S^{(2\beta\gamma)}_{12(0,1,0)}/h_\beta^2 + S^{(2\beta\gamma)}_{13(0,0,1)}/l_\gamma^2]^{(p-1)} + \frac{1}{d_1^{(p)}}[S^{(2\beta\gamma)}_{11(0,0,0)}|^{(p)} - S^{(2\beta\gamma)}_{11(0,0,0)}|^{(p-1)}] = 0 \quad (42)$$

$$S^{(1\beta\gamma)}_{11(0,0,0)}|^{(p)} = \tfrac{1}{2}S^{(2\beta\gamma)}_{11(0,0,0)}|^{(p)} + \tfrac{1}{2}S^{(2\beta\gamma)}_{11(0,0,0)}|^{(p-1)} + 3d_2^{(p)}[S^{(2\beta\gamma)}_{12(0,1,0)}/h_\beta^2 + S^{(2\beta\gamma)}_{13(0,0,1)}/l_\gamma^2]^{(p)} -$$

$$3d_2^{(p-1)}[S^{(2\beta\gamma)}_{12(0,1,0)}/h_\beta^2 + S^{(2\beta\gamma)}_{13(0,0,1)}/l_\gamma^2]^{(p-1)} \quad (43)$$

while the equations that ensure traction continuity between individual subcells associated with the x_2 and x_3 directions, eqns (20b) and (20c), are given by

$$[S^{(\alpha 1\gamma)}_{12(0,1,0)}/h_1 + S^{(\alpha 2\gamma)}_{12(0,1,0)}/h_2]^{(p)} = 0 \quad (44)$$

$$[S^{(\alpha\beta 1)}_{13(0,0,1)}/l_1 + S^{(\alpha\beta 2)}_{13(0,0,1)}/l_2]^{(p)} = 0 \quad (45)$$

$$S^{(\alpha 1\gamma)}_{22(0,0,0)}|^{(p)} = S^{(\alpha 2\gamma)}_{22(0,0,0)}|^{(p)} \quad (46)$$

$$S^{(\alpha\beta 1)}_{33(0,0,0)}|^{(p)} = S^{(\alpha\beta 2)}_{33(0,0,0)}|^{(p)}. \quad (47)$$

We note that eqns (21b) and (21c) are identically satisfied by the chosen displacement field representation due to the periodic character of the composite material in the x_2–x_3 plane. For a detailed derivation of eqns (42)–(47), see section 3 of Appendix B in Aboudi *et al.* (1994b).

Equations (42)–(47) provide us with twenty-four additional relations among the zeroth-order and first-order stresses. These relations, together with eqn (41), can be expressed in terms of the unknown coefficients $U_1^{(\alpha\beta\gamma)}, \ldots, \phi_1^{(\alpha\beta\gamma)}, \ldots, \psi_3^{(\alpha\beta\gamma)}$, and the appropriate $R^{(\alpha\beta\gamma)}_{ij(l,m,n)}$ coefficients, by making use of eqns (35)–(40), providing a total of 32 of the required 56 equations necessary for the determination of these coefficients in the pth cell.

2.4.3. *Displacement continuity equations.* The additional 24 relations necessary to determine the unknown coefficients in the displacement field expansion are subsequently obtained by imposing displacement continuity conditions on an average basis at each subcell and cell interface. The continuity of displacements at each subcell interface of the pth cell, eqns (22a) through (22c), is satisfied by the following conditions

$$[w_1^{(1\beta\gamma)} + \tfrac{1}{2}d_1^{(p)}\phi_1^{(1\beta\gamma)} + \tfrac{1}{4}d_1^{(p)2}U_1^{(1\beta\gamma)}]^{(p)} = [w_1^{(2\beta\gamma)} - \tfrac{1}{2}d_2^{(p)}\phi_1^{(2\beta\gamma)} + \tfrac{1}{4}d_2^{(p)2}U_1^{(2\beta\gamma)}]^{(p)} \quad (48)$$

$$[w_1^{(\alpha 1\gamma)} + \tfrac{1}{4}h_1^2 V_1^{(\alpha 1\gamma)}]^{(p)} = [w_1^{(\alpha 2\gamma)} + \tfrac{1}{4}h_2^2 V_1^{(\alpha 2\gamma)}]^{(p)} \quad (49)$$

$$h_1\chi_2^{(\alpha 1\gamma)}|^{(p)} = -h_2\chi_2^{(\alpha 2\gamma)}|^{(p)} \quad (50)$$

$$[w_1^{(\alpha\beta 1)} + \tfrac{1}{4}l_1^2 W_1^{(\alpha\beta 1)}]^{(p)} = [w_1^{(\alpha\beta 2)} + \tfrac{1}{4}l_2^2 W_1^{(\alpha\beta 2)}]^{(p)} \quad (51)$$

$$l_1\psi_3^{(\alpha\beta 1)}|^{(p)} = -l_2\psi_3^{(\alpha\beta 2)}|^{(p)} \quad (52)$$

while the continuity of displacements between neighboring cells in the FG direction, eqn (23a), requires that

$$[w_1^{(1\beta\gamma)} - \tfrac{1}{2} d_1^{(p+1)} \phi_1^{(1\beta\gamma)} + \tfrac{1}{4} d_1^{(p+1)2} U_1^{(1\beta\gamma)}]^{(p+1)} = [w_1^{(2\beta\gamma)} + \tfrac{1}{2} d_2^{(p)} \phi_1^{(2\beta\gamma)} + \tfrac{1}{4} d_2^{(p)2} U_1^{(2\beta\gamma)}]^{(p)}. \quad (53)$$

The displacement continuity between neighboring cells in the x_2 and x_3-directions, eqns (23b) and (23c), is automatically satisfied by the chosen displacement field representation which reflects the periodic character of the composite in these directions. For a detailed derivation of eqns (48)–(53), see section 4 of Appendix B in Aboudi *et al.* (1994b).

2.4.4. *Governing equations for the unknown coefficients in the displacement expansion.* The equilibrium equations, eqn (41), together with the traction and displacement continuity equations, eqns (42)–(47) and eqns (48)–(53), respectively, form altogether 56 equations in the 56 unknowns $w_1^{(\alpha\beta\gamma)}, \phi_1^{(\alpha\beta\gamma)}, U_1^{(\alpha\beta\gamma)}, V_1^{(\alpha\beta\gamma)}, W_1^{(\alpha\beta\gamma)}, \chi_2^{(\alpha\beta\gamma)}, \psi_3^{(\alpha\beta\gamma)}$, which govern the equilibrium of a subcell $(\alpha\beta\gamma)$ within the pth cell in the interior at the current load increment. As previously discussed in Aboudi *et al.* (1994b), a different treatment must be adopted for the boundary cells $p = 1$ and $p = M$. For $p = 1$, eqns (41), (44)–(47), and the displacement continuity relations, eqns (48) through (53), are operative, whereas eqns (42) and (43), which follow from the continuity of tractions between a given cell and the preceding one, are not applicable. These eight equations must be replaced by the conditions of continuity of tractions at the interior interfaces of the cell $p = 1$ and by the applied normal stress at $x_1 = 0$, eqn (24). Applying the traction continuity condition at the interface $\bar{x}_1^{(1)} = d_1^{(1)}/2, \bar{x}_1^{(2)} = -d_2^{(1)}/2$ between the subcells $(1, \beta, \gamma)$ and $(2, \beta, \gamma)$ within the cell $p = 1$ in an average sense

$$\frac{1}{4}\int_{-1}^{1}\int_{-1}^{1} \sigma_{11}^{(1\beta\gamma)}\, d\zeta_2\, d\zeta_3 = \frac{1}{4}\int_{-1}^{1}\int_{-1}^{1} \sigma_{11}^{(2\beta\gamma)}\, d\zeta_2\, d\zeta_3$$

produces

$$\sum_{l=0}^{\infty} \sqrt{(1+2l)}\, \tau_{11(l,0,0)}^{(1\beta\gamma)} P_l(+1) = \sum_{l=0}^{\infty} \sqrt{(1+2l)}\, \tau_{11(l,0,0)}^{(2\beta\gamma)} P_l(-1) \quad (54)$$

for $\beta, \gamma = 1, 2$. The boundary condition $\sigma_{11}^{(1\beta\gamma)} = f(t)$ at $\zeta_1^{(1)} = -1$ given by eqn (24) is also applied in an average sense, i.e.

$$\frac{1}{4}\int_{-1}^{1}\int_{-1}^{1} \sigma_{11}^{(1\beta\gamma)}\, d\zeta_2\, d\zeta_3 = f(t).$$

Expressing the normal traction $\sigma_{11}^{(1\alpha\beta)}$ in terms of the Legendre polynomial expansion, and then performing the indicated integration, yields

$$\sum_{l=0}^{\infty} \sqrt{(1+2l)}(-1)^l \tau_{11(l,0,0)}^{(1\beta\gamma)} = f(t) \quad \text{for} \quad \beta = 1,2; \quad \gamma = 1,2. \quad (55)$$

For the cell $p = M$, the previously derived governing equations are operative except for the four relations given by eqn (53) which are obviously not applicable. These are replaced by the condition that the surface $x_1 = H$ is rigidly clamped (say), eqn (25). Consequently, the governing equations at both interior and boundary cells form a system of $56M$ linear algebraic equations in the field variables of the cells along $0 \leqslant x_1 \leqslant H$ at the current instant of loading. The final form of this system of equations is symbolically represented below

$$\mathbf{K}\,\mathbf{U} = \mathbf{f} + \mathbf{g} \quad (56)$$

where the structural stiffness matrix $\mathbf{K}$ contains information on the geometry and thermomechanical properties of the individual subcells $(\alpha\beta\gamma)$ in the M cells spanning the

thickness of the FG plate. The displacement coefficient vector **U** contains the unknown coefficients that describe the displacement field in each subcell, i.e. $\mathbf{U} = (\mathbf{U}_1^{(111)}, \ldots, \mathbf{U}_M^{(222)})$ where $\mathbf{U}_p^{(\alpha\beta\gamma)} = (w_1, \phi_1, U_1, V_1, W_1, \chi_2, \psi_3)_p^{(\alpha\beta\gamma)}$, and the mechanical force vector **f** contains information on the mechanical boundary conditions and the thermal loading effects generated by the applied temperature. In addition, the inelastic force vector **g** appearing on the right hand side of eqn (56) contains the inelastic effects given in terms of the integrals of the inelastic strain distributions that are represented by the coefficients $R_{ij(l,m,n)}^{(\alpha\beta\gamma)}$. These integrals depend implicitly on the elements of the displacement coefficient vector **U**, requiring an incremental solution of eqn (56) at each point along the loading path.

2.4.5. *Solution of the governing equations for the unknown coefficients.* The choice of an appropriate technique for the solution of eqn (56) depends on the inelastic constitutive model employed to calculate the inelastic strain distributions in each subcell from which the coefficients $R_{ij(l,m,n)}^{(\alpha\beta\gamma)}$ can be generated. For instance, if the classical incremental plasticity (Prandtl–Reuss) equations are employed to model the inelastic response of the matrix phase, then Mendelson's iterative method of successive elastic solutions is an appropriate technique for the determination of the plastic strains needed in the solution of eqn (56) at each increment of the applied load (Mendelson, 1983). This method has recently been employed by Pindera *et al.* (1993a,b) in investigating the thermo-plastic response of unidirectional metal matrix composites subjected to axisymmetric loading for those situations where rate effects can be neglected. An advantage of this solution technique is its efficiency and relative quick convergence even for relatively large load increments (Williams and Pindera, 1994). If, on the other hand, a unified viscoplastic constitutive theory is employed to model the inelastic response of the matrix phase, then either an implicit or an explicit technique can be employed to integrate the viscoplastic rate equations at each increment of the applied load. The integration of viscoplastic constitutive equations, however, can require a substantial computational effort due to the potentially stiff behavior of this class of equations.

In the present framework, two constitutive theories are employed to describe the inelastic response of the matrix phase, namely the Bodner–Partom unified viscoplasticity theory and the classical incremental plasticity theory. The plasticity theory is employed to efficiently model the inelastic constitutive response of the matrix phase when rate effects can be neglected, whereas the more computationally intensive Bodner–Partom theory is employed for those situations where rate-dependent deformation must be taken into account. It should be noted that the present formulation is sufficiently general to accommodate other types of unified viscoplasticity theories.

Bodner–Partom unified viscoplasticity theory. The version of the Bodner–Partom theory employed in generating the components of the inelastic force vector **g** in eqn (56) is limited to viscoplastic materials that exhibit isotropic hardening. While the theory, in general, models rate-dependent behavior of metals at elevated temperatures, it is particularly suitable for modeling rate-dependent plastic deformation at different loading rates.

According to the Bodner–Partom theory, the viscoplastic strain rate in the matrix phase is expressed as (omitting the superscripts $(\alpha\beta\gamma)$ associated with a particular matrix subcell)

$$\dot{\varepsilon}_{ij}^{\mathrm{I}} = \Lambda s_{ij} \tag{57}$$

where Λ is the flow rule function of the matrix material and s_{ij} are the deviatoric stress components, that is $s_{ij} = \sigma_{ij} - \sigma_{kk}\,\delta_{ij}/3$. The explicit form of the flow rule function is given by

$$\Lambda = D_0 \exp\{-\hat{n}[Z^2/(3J_2)]^n\}/\sqrt{J_2} \tag{58}$$

where $\hat{n} = (n+1)/2n$, and $J_2 = \mathrm{s}\cdot\mathrm{s}/2$ is the second invariant of the deviatoric stresses. D_0

and n are inelastic parameters, and Z is a state variable whose evolution is given for an isotropic hardening material by

$$\dot{Z} = \frac{m}{Z_0}(Z_1 - Z)\,\dot{W}_p \tag{59}$$

where $\dot{W}_p$ is the plastic work rate per unit volume.

In the above equations, the five parameters D_0, Z_0, Z_1, n and m have the following meaning. D_0 is the limiting strain rate in shear for large values of the second stress invariant J_2; Z_0 is the initial value of the hardening variable Z which is related to the yield stress of the material in simple tension; Z_1 is the saturation value of the hardening variable for large values of stresses; m is a parameter that controls the rate of work-hardening of the material; and n is a parameter that controls the rate sensitivity of the material. More information regarding the meaning and physical interpretation of these parameters can be found in Bodner (1987) and Aboudi (1991).

The solution of eqn (56) is generated at each increment of the applied thermal load as follows. First, the viscoplastic strain increments that result from an imposed thermal load increment are determined at a number of points within each subcell using an explicit forward Euler integration scheme based on the known state of deformation. These increments are then used to calculate the current inelastic strain distributions in each subcell needed to determine the coefficients $R_{ij(l,m,n)}^{(\alpha\beta\gamma)}$, and thus the elements of the inelastic force vector $\mathbf{g}$. The knowledge of the current inelastic force vector allows one to determine the current values of the displacement field vector $\mathbf{U}$ by solving eqn (56), and thus the current stress and strain states. The thermal load is incremented and the entire process repeated.

The magnitude of the applied thermal load increment is governed by the imposed rate of change of the temperature profile with respect to time and the magnitude of the time increment used to integrate the viscoplastic constitutive equations. The explicit forward Euler integration scheme presently employed requires the time increment to be sufficiently small so as to guarantee convergence of the integration process.

Classical incremental plasticity theory. In the classical incremental plasticity theory, the plastic strain increment is derived from a von Mises yield condition of the form

$$F = \tfrac{1}{2}s_{ij}s_{ij} - \tfrac{1}{3}\bar{\sigma}^2(\bar{\varepsilon}^p, T) = 0 \tag{60}$$

where the effective yield stress $\bar{\sigma}$ is a function of both the effective plastic strain $\bar{\varepsilon}^p$ and temperature T. Using the associated flow rule, the plastic strain increment at any point in the matrix phase is thus

$$\mathrm{d}\varepsilon_{ij}^p = \frac{\partial F}{\partial s_{ij}}\mathrm{d}\lambda = s_{ij}\,\mathrm{d}\lambda \tag{61}$$

where $\mathrm{d}\lambda > 0$ for plastic loading, and $\mathrm{d}\lambda \leqslant 0$ for neutral loading or unloading. The proportionality constant $\mathrm{d}\lambda$ is obtained from a consistency condition that ensures that the stress vector remains on the yield surface during plastic loading, and is given in terms of the elastic stiffness elements, stresses, elastic strains and the strain-hardening characteristics (Pindera *et al.*, 1993a). This form of the incremental plasticity equations was employed in previous investigations and found to yield generally good convergence. For materials with very low rates of strain-hardening however, difficulties can be encountered using this form of the incremental plasticity equations. To ensure convergence of the iterative scheme for a wide class of materials in a wide temperature range, so-called plastic strain–total strain plasticity relations were employed in the present investigation by rewriting eqn (61) in terms of total strains without recourse to the stresses (Mendelson, 1983; Pindera *et al.*, 1993b). In this formulation of the incremental plasticity equations, the plastic strain increments are now given in terms of so-called modified total strain deviators e_{ij}

$$\mathrm{d}\varepsilon_{ij}^{p} = \frac{e_{ij}}{\bar{e}_{\mathrm{eff}}}\mathrm{d}\bar{\varepsilon}^{p} \tag{62}$$

where $e_{ij} = \varepsilon_{ij} - 1/3\varepsilon_{kk}\delta_{ij} - \varepsilon_{ij}^{p}|_{\mathrm{previous}}$, $\bar{e}_{\mathrm{eff}} = \sqrt{2/3 e_{ij}e_{ij}}$, and the effective plastic strain increment $\mathrm{d}\bar{\varepsilon}^{p}$ is given by

$$\mathrm{d}\bar{\varepsilon}^{p} = \bar{e}_{\mathrm{eff}} - \frac{\bar{\sigma}}{3\mu} \tag{63}$$

Herein, the elastoplastic stress–strain response of the matrix is taken to be *bilinear*, with the effective stress $\bar{\sigma}(\bar{\varepsilon}^{p}, T)$ given by

$$\bar{\sigma}(\bar{\varepsilon}^{p}, T) = \bar{\sigma}_{y}(T) + H_{p}(T)\bar{\varepsilon}^{p} \tag{64}$$

where $\bar{\sigma}_{y}(T)$ is the yield stress in simple tension and $H_{p}(T)$ is the slope of the effective stress–plastic strain curve.

The implementation of these plastic strain–total strain plasticity relations is carried out in the same manner as the classical form. That is, the yield condition is first checked at each point within the elastoplastic material to determine whether the material continues to load elastically or whether it has yielded. If the material has yielded, then continued loading is ensured by $\mathrm{d}\bar{\varepsilon}^{p} > 0$ and unloading by $\mathrm{d}\bar{\varepsilon}^{p} \leqslant 0$.

The solution of eqn (56) based on the Prandtl–Reuss plasticity equations is carried out following Mendelson's iterative scheme briefly outlined next. For the given thermo-mechanical load increment, the inelastic strain at any point in each layer is expressed in terms of the strain from the preceding loading state plus an increment that results from the imposed load increment

$$\varepsilon_{ij}^{p}(\mathbf{x})|_{\mathrm{current}} = \varepsilon_{ij}^{p}(\mathbf{x})|_{\mathrm{previous}} + \mathrm{d}\varepsilon_{ij}^{p}(\mathbf{x}) \tag{65}$$

The plastic strain distribution in each subcell is subsequently determined by calculating plastic strains at 21 equally spaced locations after updating the plastic strains at these locations using eqn (65). The current values for the plastic strains at these stations are then used in determining the integrals $R_{ij(l,m,n)}^{(\alpha\beta\gamma)}$ given in eqn (33), and thus the elements of the inelastic force vector $\mathbf{g}$ in eqn (56). Updated values of the interfacial displacements are then obtained from these equations. With a knowledge of the current components of the displacement coefficient vector $\mathbf{U}$, solutions for the displacement components $u_1^{(\alpha\beta\gamma)}$, $u_2^{(\alpha\beta\gamma)}$ and $u_3^{(\alpha\beta\gamma)}$, eqns (26), at any point within each subcell are obtained, from which total strains, and their corresponding stresses, are calculated. These are then used to obtain new approximations for the plastic strain increments. The iterative process is terminated when the differences between two successive sets of plastic strain increments are less than some prescribed value.

2.4.6. *Inplane force and moment resultants.* The determination of the stress fields in the individual subcells obtained from the solution of eqn (56) allows one to generate the inplane force and moment resultants produced by the stress components in the x_2–x_3 plane (see Fig. 1). The inplane force and moment resultants are defined as follows

$$\mathbf{N} = \int_{-H/2}^{H/2} \boldsymbol{\sigma}(z)\,\mathrm{d}z \tag{66}$$

$$\mathbf{M} = \int_{-H/2}^{H/2} \boldsymbol{\sigma}(z) z\,\mathrm{d}z. \tag{67}$$

Changing the integration variable from z to $\zeta_1^{(\alpha)}$ we obtain:

$$\mathbf{N}^{(\beta\gamma)} = \sum_{p=1}^{M}\sum_{\alpha=1}^{2}\frac{d_\alpha^{(p)}}{2}\int_{-1}^{1}\sum_{l=0}^{\infty}\sqrt{1+2l}\,\tau_{(l,0,0)}^{(\alpha\beta\gamma)}P_l(\zeta_1^{(\alpha)})\,\mathrm{d}\zeta_1^{(\alpha)} = \sum_{p=1}^{M}\sum_{\alpha=1}^{2}d_\alpha^{(p)}\tau_{(0,0,0)}^{(\alpha\beta\gamma)} \tag{68}$$

$$\mathbf{M}^{(\beta\gamma)} = \sum_{p=1}^{M}\sum_{\alpha=1}^{2}\frac{d_\alpha^{(p)}}{2}\int_{-1}^{1}\left(x_1^{(p)}+\frac{d_\alpha^{(p)}}{2}-\frac{H}{2}+\frac{d_\alpha^{(p)}}{2}\zeta_1^{(\alpha)}\right)\times\sum_{l=0}^{\infty}\sqrt{1+2l}\,\tau_{(l,0,0)}^{(\alpha\beta\gamma)}P_l(\zeta_1^{(\alpha)})\,\mathrm{d}\zeta_1^{(\alpha)}$$

$$= \sum_{p=1}^{M}\sum_{\alpha=1}^{2}\frac{d_\alpha^{(p)}}{2}\left[2\left(x_1^{(p)}+\frac{d_\alpha^{(p)}}{2}-\frac{H}{2}\right)\tau_{(0,0,0)}^{(\alpha\beta\gamma)}+\frac{d_\alpha^{(p)}}{\sqrt{3}}\tau_{(1,0,0)}^{(\alpha\beta\gamma)}\right] \tag{69}$$

where

$$x_1^{(p)} = \sum_{k=1}^{p-1}(d_1^{(k)}+d_2^{(k)}) \quad \text{for } \alpha = 1$$

or

$$x_1^{(p)} = \sum_{k=1}^{p-1}(d_1^{(k)}+d_2^{(k)})+d_1^{(p)} \quad \text{for } \alpha = 2$$

and so

$$\mathbf{N} = \frac{1}{(h_1+h_2)(l_1+l_2)}\sum_{\beta,\gamma=1}^{2}h_\beta l_\gamma\mathbf{N}^{(\beta\gamma)} \tag{70}$$

$$\mathbf{M} = \frac{1}{(h_1+h_2)(l_1+l_2)}\sum_{\beta,\gamma=1}^{2}h_\beta l_\gamma\mathbf{M}^{(\beta\gamma)}. \tag{71}$$

3. APPLICATIONS

The approach outlined in the foregoing is employed to investigate the response of metal matrix composite (MMC) plates subjected to a thermal gradient in the through-the-thickness direction (i.e. in the FG direction) in the presence of temperature-dependent inelastic behavior of the constituents. The objective is to quantify the effect of inelasticity on the response of uniformly and nonuniformly graded composites at the micromechanical and macromechanical levels. To accomplish this, the results of a purely elastic analysis presented earlier by Aboudi *et al.* (1993) will be compared and contrasted with the results of the inelastic analysis. In addition, application of the theory developed herein to MMC plates with a thermal barrier coating is also presented. Results for different distributions of ceramic inclusions in a metallic matrix protected by a ceramic thermal barrier coating (TBC) are compared with the results generated for configurations laminated with homogeneous materials in order to demonstrate the influence of graded architectures on the internal temperature and stress distributions, and the resulting inplane force and moment resultants.

Consequently, two types of configurations are considered herein. In the first case, unidirectional composite plates consisting of continuous SiC fibers oriented in the x_3 direction (see Fig. 1) and embedded in a titanium matrix are analyzed in the presence of various through-the-thickness thermal gradients. Configurations with three and ten through-the-thickness continuous fibers, with uniform and nonuniform spacing, are considered with the emphasis on the comparison of elastic and inelastic analyses. This includes internal stress fields and the resulting inplane force and moment resultants. The imposed temperature gradient across the plate's thickness is 500°C, with the temperature T_T at the top surface of the composite ($x_1 = 0$) higher relative to the temperature T_B at the bottom surface ($x_1 = H$). Two reference T_B temperatures were employed for the configuration with

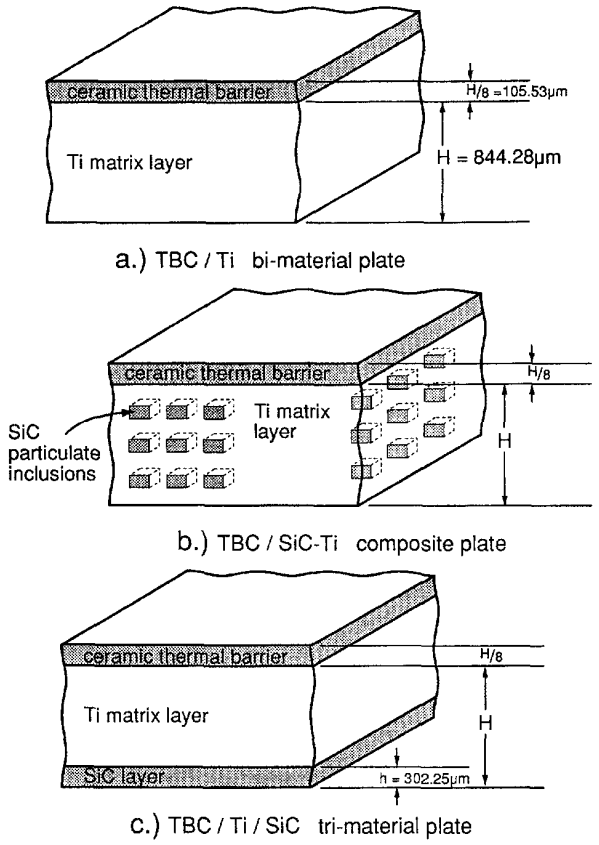

Fig. 3. Metal matrix composite plate configurations protected by a ceramic thermal barrier coating (TBC) : (a) TBC/Ti bi-material plate ; (b) TBC/SiC-Ti composite plate ; (c) TBC/Ti/SiC tri-material plate.

three through-the-thickness fibers, namely 21°C and 400°C, while six reference temperatures were employed for the configuration with ten through-the-thickness fibers, namely 21°C, 100°C, 200°C, 300°C, 350°C and 400°C. The two configurations are constrained from deforming due to the applied thermal loading by imposing mixed boundary conditions at the bottom surface that simulate honeycomb-type constraint (i.e. zero displacement over a portion of the unit cell and zero traction over the remaining part). At the top surface, the normal traction component is required to vanish (i.e. $\sigma_{11} = 0$).

In the second case, the response of a composite plate consisting of a titanium matrix reinforced by discrete SiC inclusions and protected at the hot surface by a thin ceramic TBC was analyzed in the presence of a temperature gradient of 879°C. The designation TBC/Ti-SiC is used to describe this composite plate configuration. Three through-the-thickness rows of inclusions with uniform and nonuniform spacings were employed in the analysis for the Ti-SiC region. The applied temperature T_T at the top surface of the composite plate was 900°C while the bottom surface temperature T_B was maintained at 21°C. This configuration was constrained in the same manner as the continuously reinforced configurations without the thermal barrier coating. In order to assess the potential benefit derived from embedding particulate inclusions in the titanium layer, two additional configurations constructed with homogeneous plies were investigated. One configuration, herein called TBC/Ti bi-material plate, consisted of a thin ceramic TBC bonded to a pure titanium layer. In the other configuration, herein called TBC/Ti/SiC tri-material plate, a thin SiC layer was bonded to the bottom face of the titanium layer protected by a TBC, such that the volume ratio of the titanium and SiC plies was the same as that in the SiC inclusion-reinforced configurations. Figure 3 illustrates the three types of configurations protected by thermal barriers considered herein.

Table 1. Material properties of SiC fiber

E (GPa)	ν	α (10^{-6} m/m/°C)	κ (W/m-°C)
400.0	0.17	3.53	17.6

E and ν denote the Young's modulus and Poisson's ratio, respectively, α is the coefficient of thermal expansion, and κ is the thermal conductivity.

Table 2. Thermo-elastic material properties of Ti-6Al-4V titanium matrix

Temperature (°C)	E (GPa)	ν	α (10^{-6} m/m/°C)	κ (W/m-°C)
21	113.7	0.3	9.44	8.0
149	107.5	0.3	9.62	10.0
315	97.9	0.3	9.78	13.0
482	81.3	0.3	9.83	15.0
649	49.6	0.3	9.72	17.0
900	20.7	0.3	9.81	18.0

Table 3. Inelastic material properties of Ti-6Al-4V titanium matrix

Temperature (°C)	D_0 (sec^{-1})	Z_0 (GPa)	Z_1 (GPa)	m	n	Y (MPa)	H (GPa)
21	10,000	1.06	1.5	12.70	10.00	900	4.6
149	10,000	0.89	1.5	11.68	8.42	730	4.7
315	10,000	0.80	1.5	19.20	3.60	517	5.4
482	10,000	1.14	1.5	121.00	1.17	482	4.8
649	10,000	1.16	1.5	85.60	1.04	303	1.7
900	10,000	0.58	1.5	340.00	0.40	35	1.2

D_0, Z_0, Z_1, m, n are the Bodner–Partom viscoplastic constants, while Y and H are the yield stress in simple tension and the flow modulus, respectively.

Table 4. Thermo-elastic material properties of a porous ceramic thermal barrier coating

Temperature (°C)	E(GPa)	ν	α(10^{-6} m/m/°C)	κ(W/m − °C)
21	41	0.25	10.0	1.5
645	37	0.25	11.0	3.0
982	26	0.25	12.0	3.9

The properties of the SiC fiber/inclusion and matrix phases used in the continuously reinforced and the TBC-protected configurations are provided in Tables 1 through 3, while the properties of the ceramic thermal barrier coating are given in Table 4. The SiC fiber/inclusion phase is elastic with temperature-independent material parameters, while the titanium matrix properties are given at six different temperatures in the range 21°C to 900°C. The ceramic TBC is elastic with temperature-dependent properties specified at three different temperatures in the range 21°C to 982°C. The titanium matrix for the continuously reinforced configurations without the thermal barrier coating is modeled using the Bodner–Partom unified viscoplasticity theory. Alternatively, the same titanium matrix is modeled

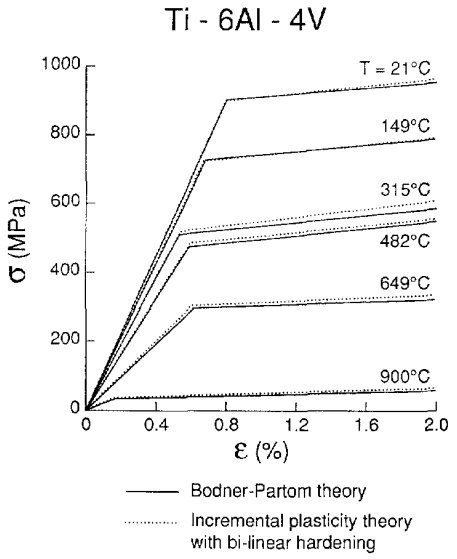

Fig. 4. Comparison of the titanium stress–strain response predicted by the Bodner–Partom unified viscoplasticity theory and the classical incremental plasticity theory.

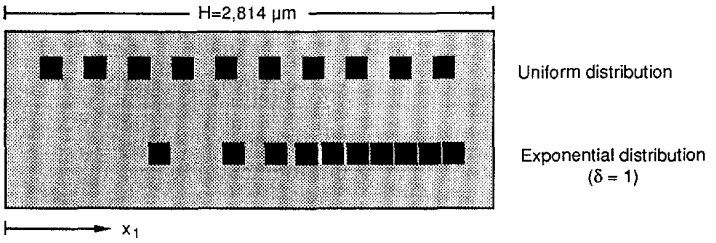

Fig. 5. Uniform and exponential ($\delta = 1$) fiber distributions along the x_1 direction in a composite with ten through-the-thickness fibers.

using the classical incremental plasticity theory for the configurations protected by the thermal barrier coating. In this case, bilinear stress–strain representation is chosen with a constant hardening slope. Figure 4 compares the predicted responses of the titanium matrix obtained from the two inelastic constitutive models. As mentioned previously, the incremental plasticity model is substantially more efficient in generating a solution to the outlined problems than the Bodner–Partom viscoplastic model and therefore is more attractive when rate-dependent effects can be neglected. The use of the two models illustrates the ease of incorporating different inelastic constitutive theories into the analytical framework outlined herein.

The nonuniform fiber and particulate inclusion distributions in the FG direction considered in the two types of configurations involve exponential spacings, Fig. 5. The exponential fiber distributions were generated by adjusting the layer thickness, $L_p = d_1^{(p)} + d_2^{(p)}$, according to the formula

$$L_p = Ae^{\delta(k-1)} + B - A \tag{72}$$

where

$$A = \frac{H - MB}{\dfrac{1-e^{\delta M}}{1-e^{\delta}} - M}.$$

In the above, $p = 1, 2, \ldots, M$, $L_1 = B = h_1 + h_2$ and $\delta = 1$ and/or 2, depending on the considered configuration, as will be described in the sequel. The total thickness of the composite is $H = 2(M-1) \times (h_1 + h_2)$, and the fiber volume fraction is then calculated from the formula

$$v_f = \frac{(M-1)d_1^{(p)2}}{H(h_1 + h_2)} \tag{73}$$

where $d_1^{(p)} = h_1$. The above distributions produce fiber concentration gradients that decrease (i.e. fiber spacing increases) with increasing x_1 coordinate. For an increasing fiber concentration gradient employed in the present analysis (i.e. decreasing fiber spacing), the mirror image of the above pattern is taken.

3.1. *Response of unidirectional composites with continuous fibers*

The inelastic response of unidirectional SiC/Ti composites reinforced with uniformly and exponentially spaced continuous fibers is compared with results from a purely elastic analysis. Comparisons of both the normal stress distributions and the inplane force and moment resultants are presented. Only the σ_{22} distributions will be presented, however, as the σ_{33} distributions exhibited similar trends, leading to the same conclusions. The σ_{22} distributions are given for the representative cross-section (RCS) containing both phases (see Fig. 1). Since in the present formulation the thermal and mechanical field quantities are uncoupled, the temperature profiles generated using elastic and inelastic analyses are identical, and thus will not be presented. Results showing the influence of internal architecture on the thermal fields have been presented elsewhere (Aboudi *et al.*, 1993; 1994a,b).

The fiber dimension $d_1^{(p)}$ for all configurations was 125.85 μm, and was obtained by ensuring that the cross-sectional area of the circular SiC fiber was equal to the cross-sectional area of the square idealization employed in the model. The horizontal cell dimension $h_1 + h_2$, which also defines the parameter B in eqn (72) for the exponentially spaced configurations, was 140.71 μm. Thus the total thickness H of the configurations with three and ten through-the-thickness fibers was 844.28 and 2,814 μm, respectively. These dimensions ensured that the fiber volume fraction was always maintained at 0.40, or 40%. For the uniformly spaced configurations, the fiber centers coincided with planes that divided the SiC/Ti composite plates into four or eleven equal plies. For the exponentially spaced configurations, the location of the fiber adjacent to the colder surface coincided with the horizontal cell dimension $B = h_1 + h_2$, whereas the remaining distances between fiber centers were obtained from eqn (72). The exponential fiber distributions were generated using $\delta = 1$ in eqn (72).

3.1.1. *Unidirectional composites with three through-the-thickness fibers.* The normal stress distributions σ_{22} obtained with the elastic and viscoplastic analysis are presented in Fig. 6 for the configuration with three through-the-thickness fibers subjected to the 500°C temperature gradient, with the reference temperature T_B at the bottom surface held at 21°C. For both the uniformly and exponentially spaced fiber distributions, Figs 6(a) and 6(b) respectively, no difference between the elastic and viscoplastic analysis is observed in the fiber and matrix phases below the first matrix-rich layer adjacent to the top surface. In these regions, the temperature relative to the reference temperature is not sufficiently large to initiate inelastic flow in the matrix phase. In the matrix layer directly adjacent to the top surface, however, the thermally-induced residual stresses are sufficiently large and the temperature-dependent matrix properties sufficiently low to induce plasticity in the matrix phase. This results in lower magnitudes of the normal stress σ_{22} predicted by the viscoplastic analysis relative to the elastic predictions.

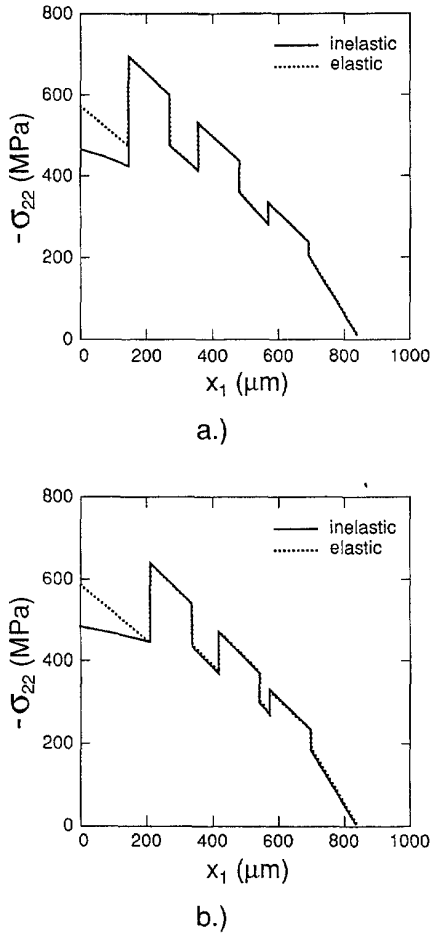

Fig. 6. Through-the-thickness normal stress σ_{22} in a unidirectional composite with three uniformly spaced (a) and exponentially spaced ($\delta = 1$) (b) fibers, in the cross-section containing both phases for $T_{ref} = 21°C$. Comparison between elastic and inelastic analysis.

Figure 7 illustrates the corresponding normal stress distributions when the reference temperature at the bottom surface is held at 400°C. In this case, the differences between elastic and inelastic analyses are substantially more pronounced, and propagate deeper into the plate. For the uniformly spaced configuration, the elastic analysis substantially overpredicts the normal stress in the matrix layer adjacent to the top surface, while in the first fiber and the adjacent matrix-rich region the differences are progressively smaller and eventually disappear at the depth of the second fiber. For the exponentially spaced configuration, similar differences in the predictions of the elastic and inelastic analyses are observed. Comparison of the stress profiles presented in Figs 6 and 7 clearly illustrate the importance of taking into account temperature-dependent properties of the constituent phases in the analysis, in addition to the inelastic effects.

Figure 8 summarizes the results for the inplane force and moment resultants generated with the elastic and inelastic analyses at the two reference temperatures for the uniformly and exponentially spaced configurations. The results are normalized by the predictions of the elastic analysis. As expected from the examination of the stress profiles, the elastic analysis overpredicts both sets of resultants, the extent of which depends on the reference temperature, the resultant quantity, and the fiber distribution. At the lower reference temperature, small differences between elastic and inelastic results for the inplane force resultants are observed in the case of both uniformly and exponentially spaced configurations. The differences in the inplane moment resultants, however, are more significant. At the higher reference temperature, the differences in the inplane force resultants increase

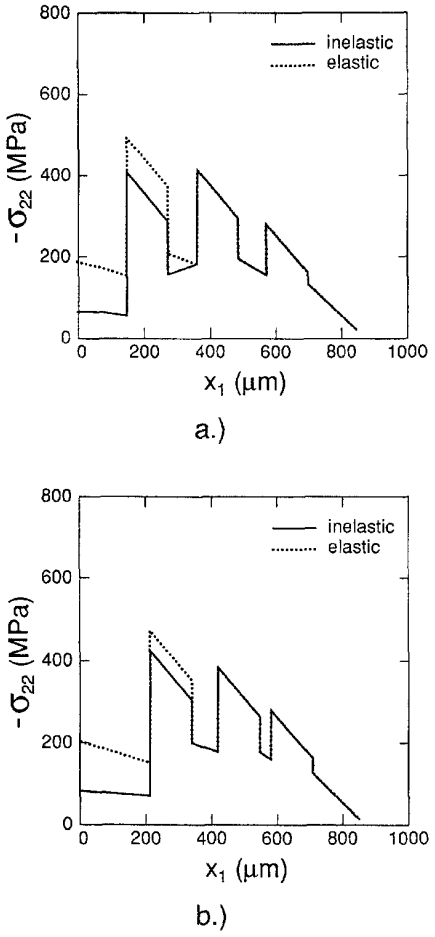

Fig. 7. Through-the-thickness normal stress σ_{22} in a unidirectional composite with three uniformly spaced (a) and exponentially spaced ($\delta = 1$) (b) fibers, in the cross-section containing both phases for $T_{ref} = 400°C$. Comparison between elastic and inelastic analysis.

somewhat, and tend to be higher for the N_2 than the N_3 resultant in both the uniformly and exponentially spaced configurations. The differences in the moment resultants, on the other hand, are very dramatic. The greatest differences occur for the M_2 moment resultant, with the exponentially spaced configuration exhibiting a greater difference than the uniformly spaced configuration. The predictions observed for the M_3 moment resultant follow similar trends.

3.1.2. *Unidirectional composites with ten through-the-thickness fibers.* The normal stress distributions σ_{22} obtained with the elastic and viscoplastic analysis are presented in Fig. 9 for the configuration with ten through-the-thickness fibers subjected to the 500°C temperature gradient, with the reference temperature T_B at the bottom surface held at 21°C. For both the uniformly and exponentially spaced fiber distributions generated with $\delta = 1$, Figs 9(a) and 9(b), respectively, no difference between the elastic and viscoplastic analysis is observed in the fiber and matrix phases at a depth greater than approximately 700 μm below the top surface of the plate. This distance corresponds to the third and first fiber from the top surface for the uniformly and exponentially spaced configurations, respectively. In the matrix regions closer to the top surface, lower magnitudes of the normal stress σ_{22} are predicted by the inelastic analysis relative to the elastic predictions. These differences are not insignificant in the matrix layer directly adjacent to the top surface and decrease with increasing distance from the top surface. Virtually no difference is observed in the normal stress σ_{22} predicted by the elastic and inelastic analyses in the fiber phase in the immediate

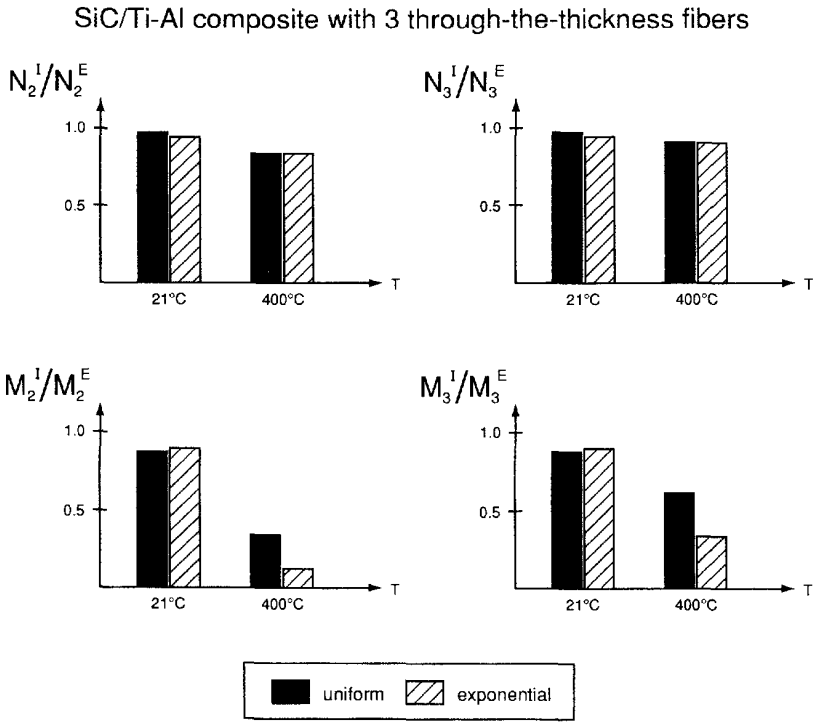

Fig. 8. Comparison of the inplane force and moment resultants obtained with elastic and inelastic analyses for a SiC/Ti composite with three through-the-thickness fibers.

vicinity of the top surface and elsewhere for both the uniformly and exponentially spaced configurations.

Figure 10 illustrates the corresponding normal stress distributions when the reference temperature at the bottom surface is held at 400°C. In this case, the differences between elastic and inelastic analyses are substantially more pronounced, and propagate deeper into the plate to approximately the same relative distance that was observed in the configurations with three through-the-thickness fibers. For both the uniformly and exponentially spaced configuration, no difference between the elastic and inelastic analyses is observed in the matrix and fiber phases at a depth approximately greater than 1200 μm below the top surface of the plate. Closer to the top surface, the elastic analysis substantially overpredicts the normal stress σ_{22} in both the matrix and fiber phases, with the differences between the elastic and inelastic analyses decreasing with increasing distance from the top surface as observed previously. Comparison of the stress profiles presented in Figures 9 and 10 again points to the importance of temperature-dependent properties of the constituent phases.

Figure 11 summarizes the results for the inplane force and moment resultants generated with the elastic and inelastic analyses at the two reference temperatures for the uniformly and exponentially spaced configurations. As in the previous case with three through-the-thickness fibers (see Fig. 8), the inplane force and moment resultants are normalized by the elastic results. The differences between the elastic and inelastic predictions follow the trends discussed for the configuration with three through-the-thickness fibers, with two important distinctions. At the lower reference temperature, differences in the inplane force and moment resultants are of the same order of magnitude (approximately 10%) for the uniformly spaced configuration. For the exponentially spaced configuration, on the other hand, the differences in the inplane force resultants decrease substantially while the differences in the moment resultants remain the same. More importantly, at the higher reference temperature the inplane moment resultants M_2 and M_3 predicted by the inelastic analysis for the exponentially spaced configuration change sign relative to the elastic predictions. In order to investigate this phenomenon further, additional results were generated at several intermediate reference temperatures. The inelastic results for the moment resultant M_2 as a

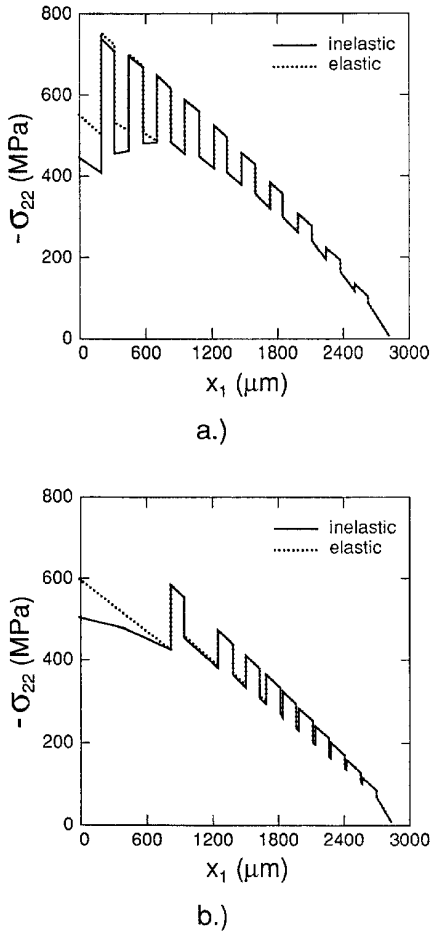

Fig. 9. Through-the-thickness normal stress σ_{22} in a unidirectional composite with ten uniformly spaced (a) and exponentially spaced ($\delta = 1$) (b) fibers, in the cross-section containing both phases for $T_{ref} = 21°C$. Comparison between elastic and inelastic analysis.

function of the reference temperature for the exponentially spaced configuration normalized by the results for the uniformly spaced configuration are presented in Fig. 12. The results indicate that the change in the sign of the moment resultant M_2 for the exponentially spaced configuration occurs above the reference (cold side) temperature of 350°C. No sign reversal is observed, however, when the inelastic effects are neglected.

3.2. *Response of thermally-protected composites with discrete inclusions*

In this section, we consider the response of a three-phase composite plate to a through-the-thickness temperature gradient. The plate consists of a ceramic TBC bonded to a titanium matrix reinforced with cubical SiC inclusions. The designation TBC/Ti-SiC is used to describe this composite plate configuration. The inclusions are distributed either uniformly or exponentially, with the exponential distributions generated using $\delta = 1$ and 2 in eqn (72). The properties of the titanium matrix and SiC inclusions are the same as the properties employed in the preceding section. The titanium matrix is modeled using the classical incremental plasticity theory. We note that the coating material is elastic with a low Young's modulus and thermal conductivity relative to those of the other constituents, and a thermal expansion coefficient comparable to that of the matrix (see Table 4). Its purpose, therefore, is to protect the portion of the Ti-SiC region subjected to an elevated temperature from excessively high temperatures.

The thickness dimension of the Ti-SiC portion of the plate is the same as in the preceding section (i.e. 844.28 μm), as is the cross-sectional area of the cubical inclusions

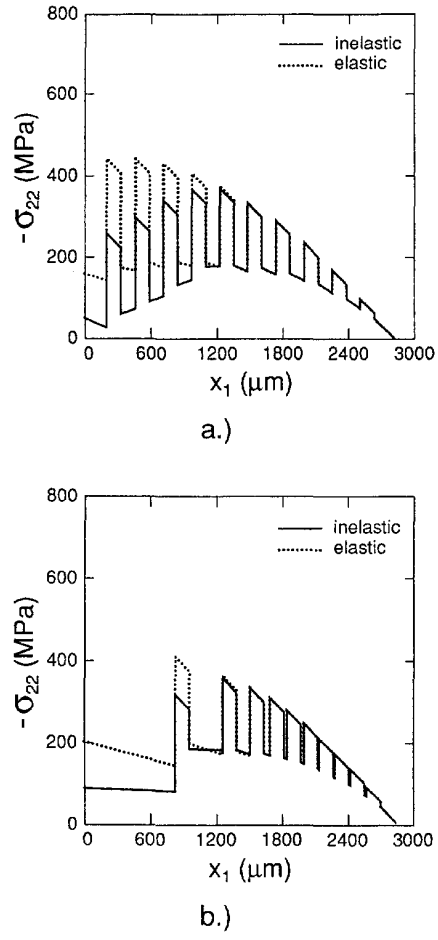

Fig. 10. Through-the-thickness normal stress σ_{22} in a unidirectional composite with ten uniformly spaced (a) and exponentially spaced ($\delta = 1$) (b) fibers, in the cross-section containing both phases for $T_{ref} = 400°C$. Comparison between elastic and inelastic analysis.

defined by $d_1^{(p)} = 125.85\,\mu m$. Thus the inclusion volume content is now different than that of the unidirectionally reinforced SiC/Ti composite considered previously (i.e. 0.358 vs 0.400). The thickness of the thermal barrier coating is one eighth that of the thickness of the Ti-SiC region, or 105.53 μm (see Fig. 3). The top surface is subjected to the temperature T_T of 900°C while the bottom surface is maintained at the temperature T_B of 21°C. Thus the total temperature gradient is now almost twice as high as in the previously considered continuously reinforced SiC/Ti composite plates without the thermal barrier coating. The presence of the low conductivity thermal barrier, however, will substantially reduce the actual thermal gradient in the Ti-SiC region of the three-phase composite plate, making it possible to draw some correlation between the two sets of results.

The response of the thermally-protected TBC/Ti-SiC configurations reinforced with uniformly and exponentially spaced inclusions predicted by the inelastic analysis is compared with a purely elastic response. Comparison for both the normal stress distributions and the inplane force and moment resultants is presented. Only the σ_{22} distributions will be presented given the same microstructure of the composite plate when viewed from the x_2 and x_3 directions. These stress distributions are given in the RCS containing both phases as well as in the RCS containing matrix only (see Fig. 1). The results are also compared with the response of a thermally-protected pure titanium matrix without the inclusion phase (TBC/Ti bi-material plate), and a thermally-protected sandwich plate consisting of homogeneous titanium and SiC plies (TBC/Ti/SiC tri-material plate). This comparison is carried out in order to illustrate the advantages of employing uniformly and nonuniformly

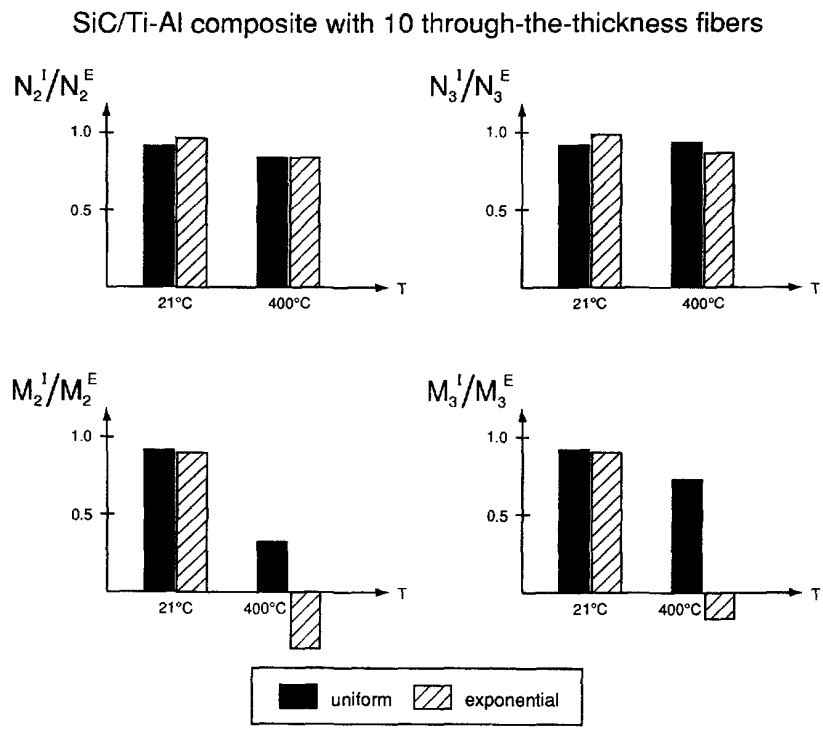

Fig. 11. Comparison of the inplane force and moment resultants obtained with elastic and inelastic analyses for a SiC/Ti composite with ten through-the-thickness fibers.

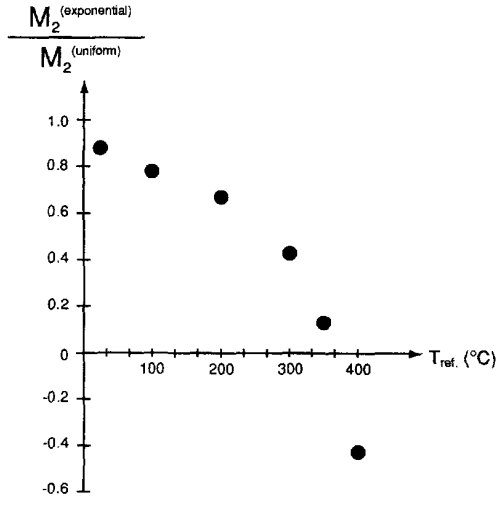

Fig. 12. Normalized moment resultant $M_2^{exponential}/M_2^{uniform}$ as a function of the reference temperature in a unidirectional composite with ten through-the-thickness fibers predicted by the inelastic analysis.

spaced two-phase microstructures to control the internal stress and plastic strain distributions with the objective of reducing the bending moment resultants.

As the first step, in Fig. 13 we present the temperature distributions in three of the five configurations protected by the same thermal barrier coating in the RCS that includes both phases. The three configurations include the TBC/Ti bi-material plate, the TBC/Ti/SiC tri-material plate, and the TBC/Ti-SiC composite plate with exponentially spaced SiC inclusions generated with $\delta = 2$. The temperature distributions for the TBC/Ti-SiC configuration with uniformly and exponentially spaced inclusions with $\delta = 1$ are not substantially different from that of the $\delta = 2$ configuration and thus are not included in the

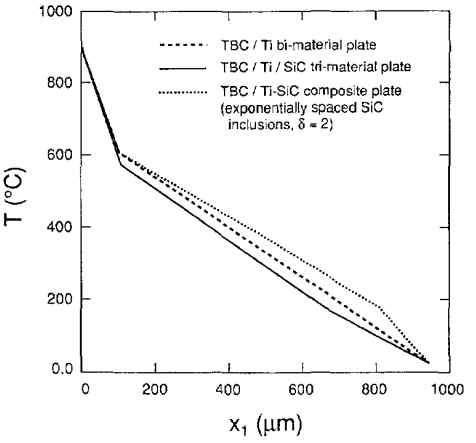

Fig. 13. Through-the-thickness temperature distributions in a TBC/Ti bi-material plate, TBC/Ti-SiC composite plate with three exponentially spaced inclusions, and TBC/Ti/SiC tri-material plate (see Fig. 3) for $T_{ref} = 21°C$.

figure. As is observed, the temperature distributions in the configurations laminated with homogeneous plies have a bi-linear or a tri-linear appearance, whereas the temperature distribution in the SiC inclusion-reinforced plate exhibits a quasi tri-linear appearance with slight changes in slope in the Ti-SiC region due to the different thermal conductivity between the titanium matrix and the SiC inclusions. The temperature profile of the TBC/Ti bi-material configuration is bounded by the temperature profiles of the TBC/Ti/SiC tri-material and the TBC/Ti-SiC composite configurations. When the SiC phase is in the form of a homogeneous plate bonded to the bottom surface of the titanium layer, the temperature distribution in such configurations is lower relative to the configuration consisting of the thermal coating bonded to the homogeneous titanium matrix. This is due to the higher thermal conductivity of the SiC layer relative to the titanium matrix in the low temperature range (see Tables 1 and 2) at the cold surface of the plate. Alternatively, when the SiC phase is embedded directly in the titanium matrix in the form of inclusions, the temperature profile is now higher relative to the TBC/Ti bi-material plate due to the higher effective thermal conductivity of the Ti-SiC composite region exposed to the elevated temperature. As will be seen, this is an important result that will have a direct bearing on the favorable redistribution of the internal stresses in the Ti-SiC region of the TBC/Ti-SiC composite plate when compared to the stress distribution in the Ti region of either the TBC/Ti bi-material or TBC/Ti/SiC tri-material plate.

The normal stress σ_{22} distributions produced by the temperature profiles presented in Fig. 13 based on the inelastic analysis are compared with the corresponding elastic results for four of the five configurations in Fig. 14. In the TBC/Ti bi-material plate, Fig. 14(a), one observes dramatic differences between the elastic and inelastic results in the titanium matrix directly adjacent to the thermal barrier coating, suggesting significant plastic flow that leads to significant reduction in the normal stress when plasticity is taken into account. These differences slowly decrease with increasing distance from the thermal barrier coating, but never fully vanish. Similar trends are observed for the TBC/Ti/SiC tri-material plate in Fig. 14(b). For the uniformly spaced TBC/Ti-SiC composite plate configuration, Fig. 14(c), substantial differences also are observed between the inelastic and elastic analyses in the matrix region next to the thermal barrier coating. However, no differences are observed in the fiber phases. Both elastic and inelastic analyses predict identical stress distributions starting from the second SiC inclusion from the thermal barrier. This is similar to the normal stress distributions observed in the continously-reinforced SiC/Ti composites discussed previously. The normal stress profiles for the exponentially spaced TBC/Ti-SiC composite plate configuration with $\delta = 2$, Fig. 14(d), follow those of the uniformly spaced configuration. The stress profiles of the exponentially spaced configuration with $\delta = 1$ are shifted relative to the profiles in Fig. 14(d), but otherwise exhibit the same pattern.

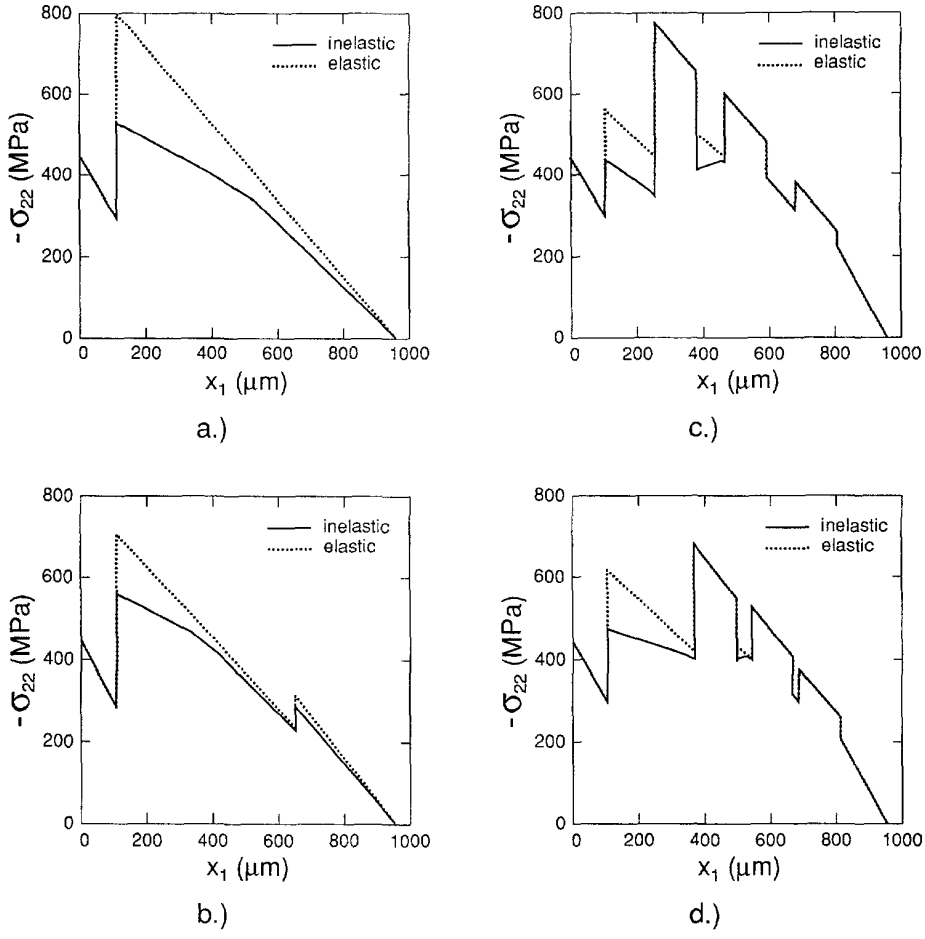

Fig. 14. Through-the-thickness normal stress σ_{22} in thermally-protected composite plate configurations with different substrate microstructures in the cross-section containing both phases for $T_{ref} = 21°C$. Comparison between elastic and inelastic analysis for: (a) TBC/Ti bi-material plate; (b) TBC/Ti/SiC tri-material plate; (c) TBC/SiC-Ti composite plate reinforced by three uniformly spaced SiC inclusions; (d) TBC/SiC-Ti composite plate reinforced by three exponentially spaced SiC inclusions ($\delta = 2$).

Figure 15 presents a comparison between the inplane force and moment resultants N_2 and M_2 obtained with the inelastic and elastic analysis for the five configurations in terms of the previously employed ratios (see Fig. 11). The greatest differences between elastic and inelastic results occur for the TBC/Ti bi-material plate, and are approximately the same for the inplane force and moment resultants (i.e. around 27%). For the SiC inclusion-reinforced configurations, differences on the order of 5% between inelastic and elastic analyses are observed for the inplane force resultants. For the moment resultants, on the other hand, these differences are substantially greater, and range from 16% to 20%. Exponentially spaced configurations produce greater differences than the uniformly spaced configuration. It is interesting to point out that in the case of the TBC/Ti/SiC tri-material plate, the differences in the elastic and inelastic predictions do not follow the trends observed in the uniformly and exponentially spaced configurations with increasing concentration of inclusions towards the colder surface. In particular, while the bending moment ratio for the SiC inclusion-reinforced configuration decreases with increasing inclusion concentration closer to the colder surface, implying an increasingly greater role of matrix plasticity in the matrix region adjacent to the ceramic TBC, the bending moment ratio for the tri-material configuration is actually higher relative to the exponentially reinforced configuration with $\delta = 2$. This can be explained by observing that the homogeneous SiC ply actually lowers the temperature distribution in the titanium matrix, Fig. 13, thus increasing the normal

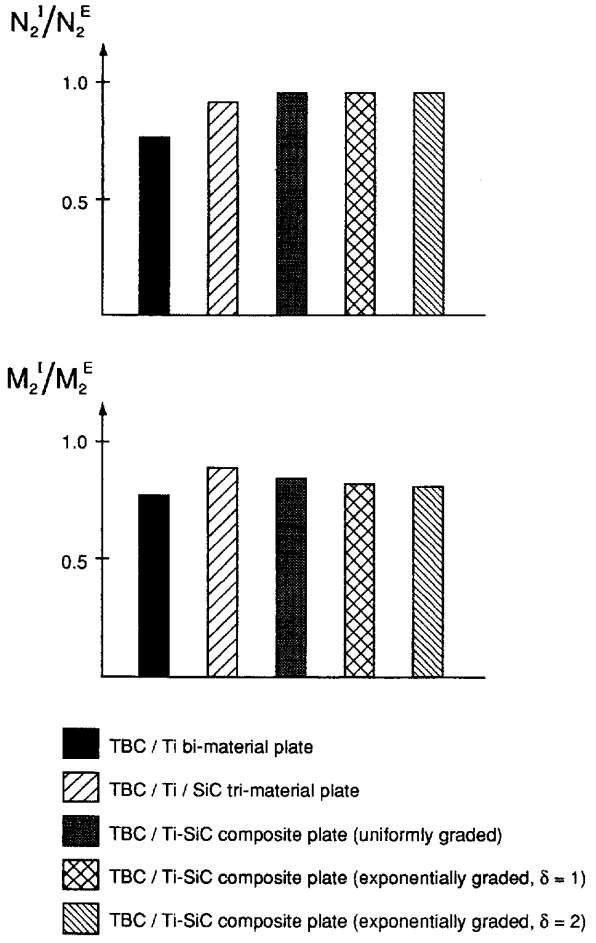

Fig. 15. Comparison of the inplane force and moment resultants obtained with elastic and inelastic analyses for the thermally-protected composite plates subjected to a through-the-thickness temperature gradient of 879°C.

stress in the titanium matrix close to the hot surface while suppressing the plastic flow due to the stiffer response of titanium at lower temperatures (see Fig. 4), as will be subsequently discussed.

Next, comparison between the inelastic stress distributions for the different configurations is presented in order to study the effect of the internal architectures on the stress and plastic strain fields, and the resulting inplane force and moment resultants. Figure 16 presents a comparison between the normal stress distributions in the bi-material and tri-material plates, and the uniformly and exponentially spaced ($\delta = 1$ and 2) configurations for the RCS containing both phases, Fig 16(a), as well as the RCS containing only the matrix phase, Fig. 16(b). The results indicate that the presence of the SiC inclusions decreases the magnitude of the normal stress in the matrix phase directly adjacent to the ceramic TBC relative to the normal stress in the bi-material and tri-material plate. In regions further away from the thermal barrier, however, the magnitude of the normal stress is now greater in the SiC particle-reinforced plate. The presence of the SiC particles, therefore, results in re-distribution of the normal stress σ_{22}, suggesting that embedding the SiC particles in the titanium matrix in the manner indicated will increase the inplane force resultants, while decreasing the moment resultants, as subsequently demonstrated.

In order to assess the role of plasticity in the redistribution of the normal stress observed in Fig. 16, effective plastic strain distributions were calculated in the bi-material and tri-material as well as the uniformly and exponentially spaced configurations. These

distributions are illustrated in Fig. 17 for both representative cross-sections. The results clearly indicate that the increase in the normal stress distribution in the TBC/Ti/SiC tri-material plate relative to the TBC/Ti bi-material plate seen in Fig. 16 is accompanied by a reduction in the plastic strain distribution. Since Fig. 13 indicates that the temperature profile in the TBC/Ti/SiC tri-material plate is lower relative to the TBC/Ti plate, the temperature-dependent properties of the titanium matrix play an important role in generating higher normal stresses and lower plastic strains in the tri-material configuration. Further, the presence of the SiC inclusions in the TBC/Ti-SiC configurations actually tends to lower the magnitudes of plastic strains in the matrix regions in both representative cross-sections relative to the pronounced plastic strains observed in the bi-material plate. Thus the normal stress reduction in the matrix phase adjacent to the ceramic coating in the TBC/Ti-SiC configurations observed in Fig. 16 is not caused by additional plasticity. This reduction is most likely due to a thermal strain relief caused by the presence of the discrete SiC inclusions with a smaller thermal expansion coefficient than the titanium matrix.

Figure 18 presents the inplane force and moment resultants for the configurations whose normal stress distributions have been given in Fig. 16. The results are normalized by the inplane force and moment resultants obtained for the TBC/Ti bi-material plate in order to demonstrate the effect of the two-phase microstructure of the Ti-SiC region on these quantities. Since the SiC inclusions are stiffer relative to the titanium matrix, the inplane

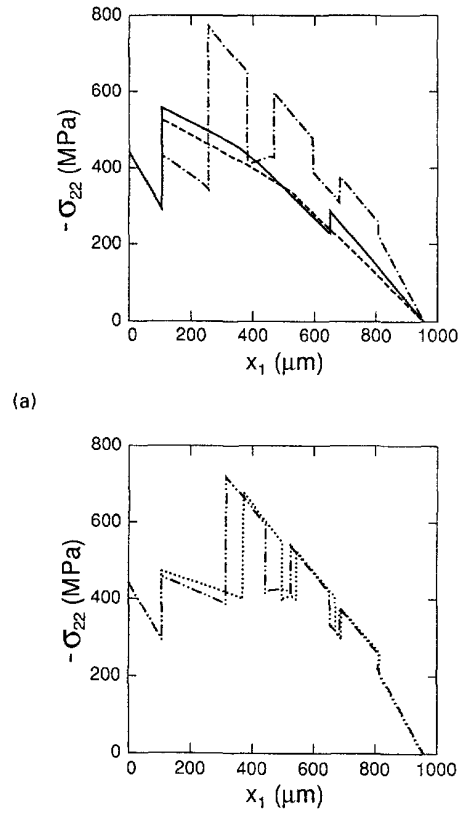

Fig. 16. Comparison between through-the-thickness normal stress σ_{22} obtained with the inelastic analysis for the thermally-protected composite configurations in: (a) the cross-section containing both phases; (b) the cross-section containing matrix only.

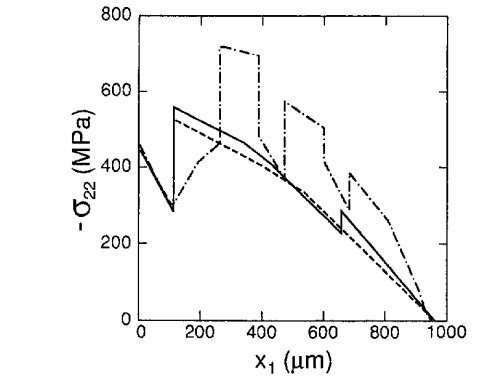

(b)

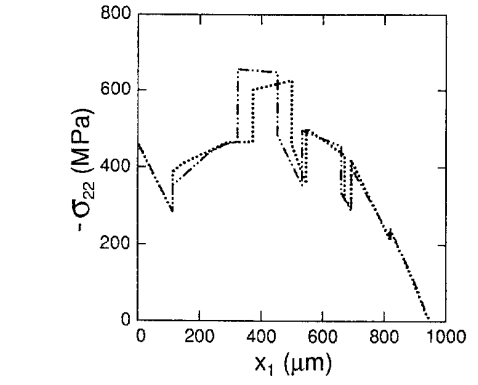

----- TBC / Ti bi-material plate

—— TBC / Ti / SiC tri-material plate

-·-·- TBC / Ti-SiC composite plate (uniformly graded)

-···- TBC / Ti-SiC composite plate (exponentially spaced SiC inclusions, δ = 1)

····· TBC / Ti-SiC composite plate (exponentially spaced SiC inclusions, δ = 2)

Fig. 16. (*Continued*).

resultant N_2 (and thus N_3) increases in the presence of the inclusion phase. More significantly, however, the presence of the SiC inclusions lowers the moment resultant M_2 (and thus M_3) relative to that of the TBC/Ti bi-material plate. As mentioned previously, this reduction is a direct result of a more favorable (i.e. more uniform) redistribution of the normal stress σ_{22} which better utilizes the load carrying capability of the matrix phase in the regions exposed to lower temperatures (i.e. regions close to the bottom face of the plate). The greatest reduction in the moment resultant occurs for the exponentially spaced configuration with $\delta = 2$ since this configuration produces a more uniform distribution of σ_{22}. It is significant that the TBC/Ti/SiC tri-material plate configuration offers a very modest reduction in the bending moment compared to that produced by both the uniformly and exponentially spaced TBC/Ti-SiC configurations.

4. CONCLUSIONS

A previously developed theory for the elastic response of thin-walled, metal matrix composites with a finite number of uniformly or nonuniformly spaced large-diameter fibers in the thickness direction subjected to a thermal gradient has been extended herein to include temperature-dependent inelastic behavior of the constituent phases. In this new approach, the microstructural and macrostructural details are *explicitly coupled* when solving the thermomechanical boundary-value problem. Coupling of local and global analyses allows one to rationally analyze the response of metal matrix composites such

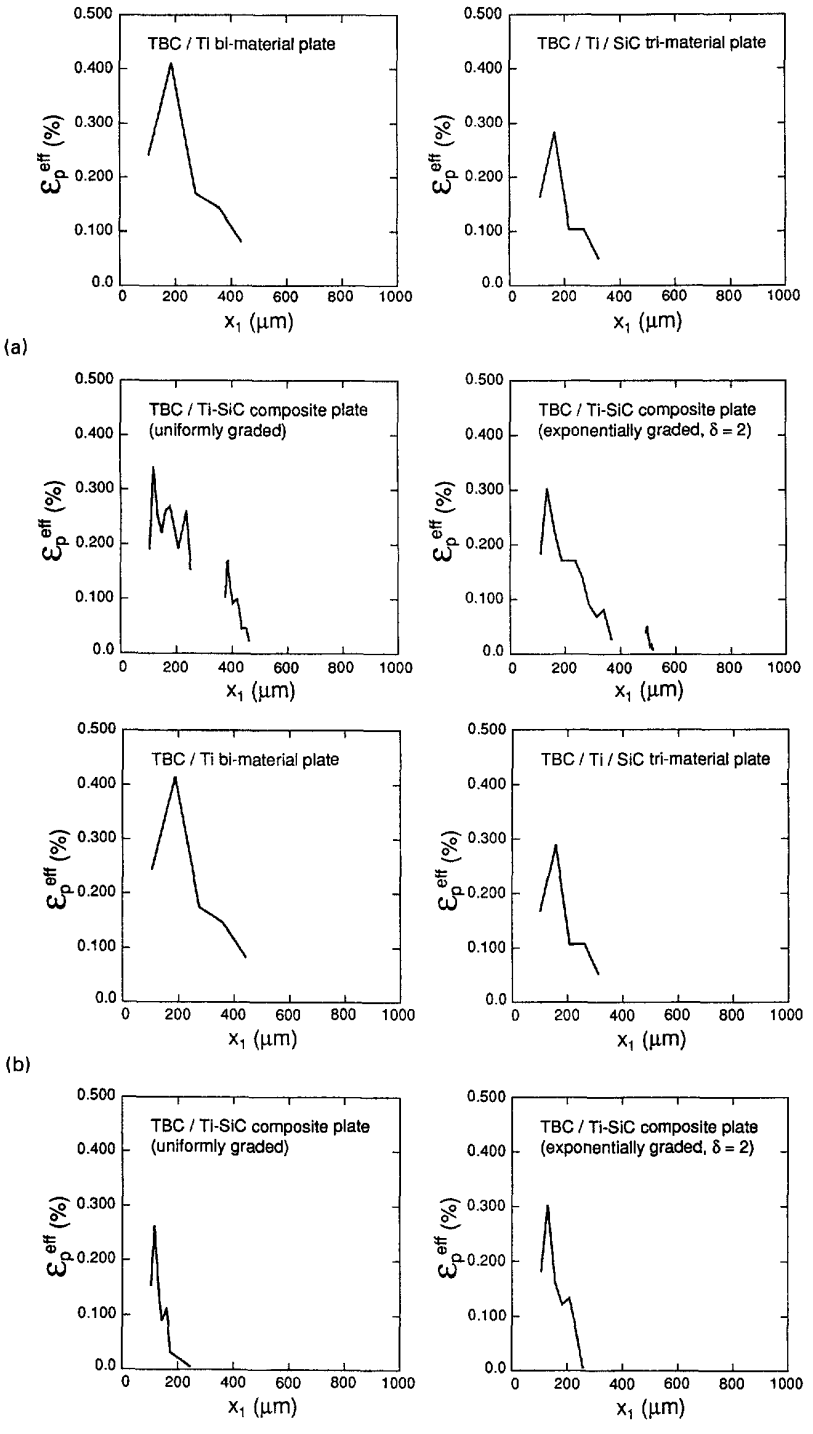

Fig. 17. Comparison between through-the-thickness effective plastic strain ε_p^{eff} obtained with the inelastic analysis for the thermally-protected composite configurations in: (a) the cross-section containing both phases;(b) the cross-section containing matrix only.

as SiC/TiAl that contain relatively few through-the-thickness fibers, as well as so-called functionally gradient composites with continuously changing properties due to nonuniform fiber spacing or the presence of several phases. For such composites, it is difficult, if not impossible, to define the representative volume element (RVE) used in the traditional micromechanical analyses currently employed to analyze this class of emerging composites.

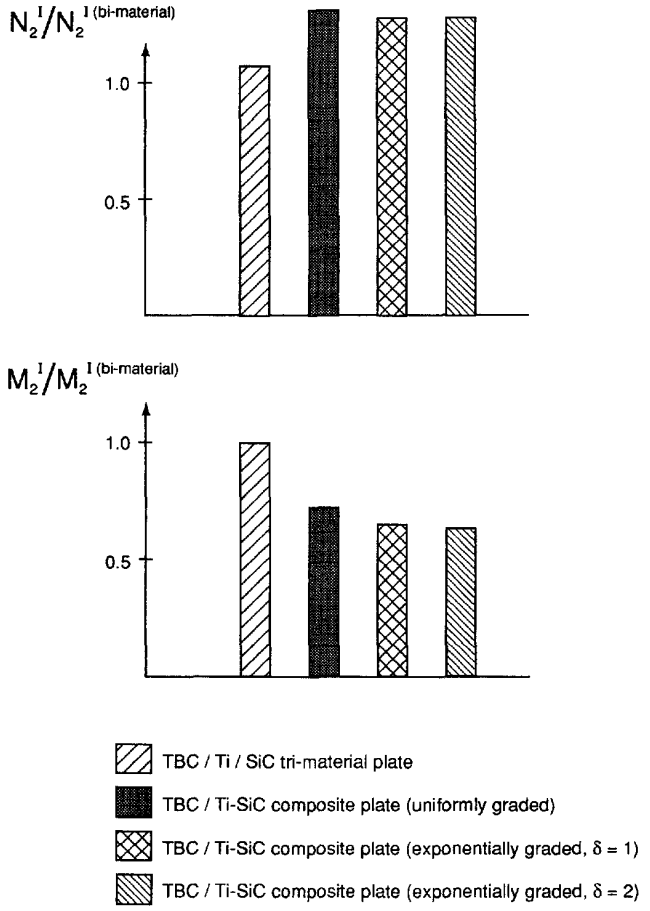

Fig. 18. Inplane force and moment resultants for the thermally-protected composite plate configurations normalized by the corresponding quantities obtained for the TBC/Ti bi-material plate.

The comparison of the internal stress and inplane force and moment resultants generated for SiC/TiAl composites using the elastic and inelastic models for the matrix phase reveals substantial differences that depend on the applied temperature gradient, the reference temperature with respect to which temperature changes are measured, and the fiber/inclusion distribution. As expected, matrix plasticity leads to a reduction in the normal stress distribution in a localized region exposed to an elevated temperature, with virtually identical normal stresses predicted by the inelastic and elastic analyses in the colder regions. The extent of the plasticity-driven reduction in the normal stress increases with increasing reference temperature applied to the cold surface of the plate, pointing to the importance of temperature-dependent properties of the metallic phase. The resulting inplane force and moment resultants are reduced proportionally, and in the case of the moment resultants may in fact reverse sign at sufficiently high reference temperatures. This occurred for the exponentially spaced configuration (with fibers concentrated near the cold surface) with ten through-the-thickness fibers when the reference temperature at the bottom surface was 400°C.

The presented results also indicate that the effectiveness of thermal barrier coatings in applications involving severe thermal gradients can be substantially increased by grading the metallic substrate using particulate inclusions. The presence of the inclusion phase produces a more favorable redistribution of the internal stress fields that more fully utilizes the load bearing capability of the matrix phase in regions exposed to lower temperatures, while potentially reducing the amount of plasticity in regions exposed to elevated temperatures.

Acknowledgements—The first two authors gratefully acknowledge the support provided by the NASA–Lewis Research Center through the grant NASA NAG 3–1377.

REFERENCES

Aboudi, J. (1991). *Mechanics of Composite Materials—A Unified Micromechanical Approach*. Elsevier, New York.

Aboudi, J., Pindera, M.-J. and Arnold, S. M. (1993). Thermoelastic response of metal matrix composites with large-diameter fibers subjected to thermal gradients. NASA TM 106301, NASA-Lewis Research Center, Cleveland, OH.

Aboudi, J., Arnold, S. M. and Pindera, M.-J. (1994a). Response of functionally graded composites to thermal gradients. *Compos. Engng* **4** (1), 1–18.

Aboudi, J., Pindera, M.-J. and Arnold, S. M. (1994b). Elastic response of metal matrix composites with tailored microstructures to thermal gradients. *Int. J. Solids Structures* **31** (10), 1393–1428.

Bodner, S. R. (1987). Review of a unified elastic–viscoplastic theory. In *Unified Constitutive Equations for Creep and Plasticity* (Edited by A. K. Miller), pp. 273–301. Elsevier, Amsterdam.

Hill, R. (1963). Elastic properties of reinforced solids: some theoretical principles. *J. Mech. Phys. Solids*, **11**, 357–372.

Malvern, L. E. (1969). *Introduction to the Mechanics of a Continuous Medium*. Prentice–Hall, Inc., Englewood Cliffs, New Jersey.

Mendelson, A. (1983). *Plasticity: Theory and Applications*. Robert E. Krieger Publishing Company, Malabar, Fl (reprint edition).

Pagano, N. J. (1974). The role of effective moduli in the elastic analysis of composite laminates. In *Composite Materials: Mechanics of Composite Materials* (Edited by G. P. Sendeckyj) pp. 1–22. Academic Press, New York.

Pindera, M.-J., Freed, A. D. and Arnold, S. M. (1993a). Effects of fiber and interfacial layer morphologies on the thermoplastic response of metal matrix composites. *Int. J. Solids Structures* **30** (9). 1213–1238. See also: Pindera, M.-J., Freed, A. D. and Arnold, S. M. (1992). Effects of fiber and interfacial layer architectures on the thermoplastic response of metal matrix composites. *NASA Technical Memorandum* 105802, NASA Lewis Research Center.

Pindera, M.-J., Salzar, R. S. and Williams, T. O. (1993b). An evaluation of a new approach for the thermoplastic response of metal-matrix composites, *Compos. Engng* **3** (12), 1185–1201.

Pindera, M.-J., Aboudi, J. and Arnold, S. M. (1994). Limitations of the uncoupled, RVE-based micromechanical approach in the analysis of functionally graded composites. *Mech. Mater.* (in press).

Yamanouchi, M., Koizumi, M., Hirai, T. and Shiota, I. (1990). *Proc. of the First International Symposium on Functionally Gradient Materials*. Sendai, Japan.

Wakashima, K. and Tsukamoto, H. (1990). Micromechanical approach to the thermomechanics of ceramic-metal gradient materials. *Proc. First International Symposium on Functionally Gradient Materials* (Edited by M. Yamanouchi, M. Koizumi, T. Hirai and I. Shiota), pp. 19–26. Sendai, Japan.

Williams, T. O. and Pindera, M.-J. (1994). Convergence rates of the method of successive elastic solutions in thermoplastic problems of a layered concentric cylinder. In *Engineering, Construction, and Operations in SPACE IV* (Edited by R. G. Galloway and S. Lokaj), pp. 348–357. ASCE, New York.

APPENDIX

The non-zero strain coefficients $e^{(\alpha\beta\gamma)}_{ij(l,m,n)}$ in the Legendre polynomial representation of the strain field in eqn (27) are given in terms of the displacement field microvariables of eqn (26) by:

$$e^{(\alpha\beta\gamma)}_{11(0,0,0)} = \phi^{(\alpha\beta\gamma)}_1$$

$$e^{(\alpha\beta\gamma)}_{11(1,0,0)} = \frac{\sqrt{3}}{2} d^{(p)}_\alpha U^{(\alpha\beta\gamma)}_1$$

$$e^{(\alpha\beta\gamma)}_{22(0,0,0)} = \chi^{(\alpha\beta\gamma)}_2$$

$$e^{(\alpha\beta\gamma)}_{33(0,0,0)} = \psi^{(\alpha\beta\gamma)}_3$$

$$e^{(\alpha\beta\gamma)}_{12(0,1,0)} = \frac{\sqrt{3}}{4} h_\beta V^{(\alpha\beta\gamma)}_1$$

$$e^{(\alpha\beta\gamma)}_{13(0,0,1)} = \frac{\sqrt{3}}{4} l_\gamma W^{(\alpha\beta\gamma)}_1.$$

The non-zero thermal stress coefficients $\tau^{T(\alpha\beta\gamma)}_{ij(l,m,n)}$ in the Legendre polynomial representation of the thermal field in eqn (29) are given in terms of the temperature field microvariables $T^{(\alpha\beta\gamma)}_l$ of eqn (3) by:

$$\tau^{T(\alpha\beta\gamma)}_{11(0,0,0)} = \Gamma^{(\alpha\beta\gamma)}_{11} T^{(\alpha\beta\gamma)}_0$$

$$\tau^{T(\alpha\beta\gamma)}_{(1,0,0)} = \Gamma^{(\alpha\beta\gamma)}_{11} \cdot \frac{d^{(p)}_\alpha}{2\sqrt{3}} T^{(\alpha\beta\gamma)}_1$$

$$\tau_{11(2,0,0)}^{T(\alpha\beta\gamma)} = \Gamma_{11}^{(\alpha\beta\gamma)} \frac{d_\alpha^{(p)2}}{4\sqrt{5}} T_2^{(\alpha\beta\gamma)}$$

$$\tau_{11(0,2,0)}^{T(\alpha\beta\gamma)} = \Gamma_{11}^{(\alpha\beta\gamma)} \frac{h_\beta^2}{4\sqrt{5}} T_3^{(\alpha\beta\gamma)}$$

$$\tau_{11(0,0,2)}^{T(\alpha\beta\gamma)} = \Gamma_{11}^{(\alpha\beta\gamma)} \frac{l_\gamma^2}{4\sqrt{5}} T_4^{(\alpha\beta\gamma)}$$

$$\tau_{22(0,0,0)}^{T(\alpha\beta\gamma)} = \Gamma_{22}^{(\alpha\beta\gamma)} T_0^{(\alpha\beta\gamma)}$$

$$\tau_{22(1,0,0)}^{T(\alpha\beta\gamma)} = \Gamma_{22}^{(\alpha\beta\gamma)} \frac{d_\alpha^{(p)}}{2\sqrt{3}} T_1^{(\alpha\beta\gamma)}$$

$$\tau_{22(2,0,0)}^{T(\alpha\beta\gamma)} = \Gamma_{22}^{(\alpha\beta\gamma)} \frac{d_\alpha^{(p)2}}{4\sqrt{5}} T_2^{(\alpha\beta\gamma)}$$

$$\tau_{22(0,2,0)}^{T(\alpha\beta\gamma)} = \Gamma_{22}^{(\alpha\beta\gamma)} \frac{h_\beta^2}{4\sqrt{5}} T_3^{(\alpha\beta\gamma)}$$

$$\tau_{22(0,0,2)}^{T(\alpha\beta\gamma)} = \Gamma_{22}^{(\alpha\beta\gamma)} \frac{l_\gamma^2}{4\sqrt{5}} T_4^{(\alpha\beta\gamma)}$$

$$\tau_{33(0,0,0)}^{T(\alpha\beta\gamma)} = \Gamma_{33}^{(\alpha\beta\gamma)} T_0^{(\alpha\beta\gamma)}$$

$$\tau_{33(1,0,0)}^{T(\alpha\beta\gamma)} = \Gamma_{33}^{(\alpha\beta\gamma)} \frac{d_\alpha^{(p)}}{2\sqrt{3}} T_1^{(\alpha\beta\gamma)}$$

$$\tau_{33(2,0,0)}^{T(\alpha\beta\gamma)} = \Gamma_{33}^{(\alpha\beta\gamma)} \frac{d_\alpha^{(p)2}}{4\sqrt{5}} T_2^{(\alpha\beta\gamma)}$$

$$\tau_{33(0,2,0)}^{T(\alpha\beta\gamma)} = \Gamma_{33}^{(\alpha\beta\gamma)} \frac{h_\beta^2}{4\sqrt{5}} T_3^{(\alpha\beta\gamma)}$$

$$\tau_{33(0,0,2)}^{T(\alpha\beta\gamma)} = \Gamma_{33}^{(\alpha\beta\gamma)} \frac{l_\gamma^2}{4\sqrt{5}} T_4^{(\alpha\beta\gamma)}.$$